Fixed-*t* analyticity as a constraint in single-energy partial-wave analyses of meson photoproduction reactions

H. Osmanović,[1,][*] M. Hadžimehmedović,[1] R. Omerović,[1] J. Stahov,[1] V. Kashevarov,[2] K. Nikonov,[2] M. Ostrick,[2]
L. Tiator,[2] and A. Švarc[3]

[1]*University of Tuzla, Faculty of Natural Sciences and Mathematics, Univerzitetska 4, 75000 Tuzla, Bosnia and Herzegovina*
[2]*Institut für Kernphysik, Johannes Gutenberg-Universität Mainz, D-55099 Mainz, Germany*
[3]*Rudjer Bošković Institute, Bijenička cesta 54, P.O. Box 180, 10002 Zagreb, Croatia*

Partial-wave amplitudes of meson photoproduction reactions are an important source of information in baryon spectroscopy. We investigate a new approach in single-energy partial-wave analyses of these reactions. Instead of using a constraint to theoretical models in order to achieve solutions which are continuous in energy, we enforce the analyticity of the amplitudes at fixed values of the Mandelstam variable t. We present an iterative procedure with successive fixed-t amplitude analyses which constrain the single-energy partial-wave analyses and apply this method to the $\gamma p \to \eta p$ reaction. We use pseudodata, generated by the EtaMAID model, to test the method and to analyze ambiguities. Finally, we present an analytically constrained partial-wave analysis using experimental data for four polarization observables recently measured at MAMI and GRAAL in the energy range from threshold to $\sqrt{s} = 1.85$ GeV.

I. INTRODUCTION

Photoproduction of pseudoscalar mesons is a powerful tool in hadron spectroscopy. Excited baryons with definite quantum numbers appear as resonances in the energy dependence of partial-wave scattering or multipole amplitudes. The complex interference pattern of these amplitudes manifests itself in four different energy- and angular-dependent helicity amplitudes and, finally, in 16 single- and double-spin observables. The inverse problem of uniquely reconstructing partial-wave amplitudes up to an overall phase from an experimentally measured subset of these observables is an important prerequisite for a reliable isolation of resonances and their separation from background.

Experimentally, major progress was observed during the past two decades due to the extensive developments at Electron Stretcher and Accelerator (ELSA), GRenoble Anneau Accélérateur Laser (GRAAL), Jefferson Laboratory (JLab), and Mainz Microtron (MAMI) in beam and target polarization techniques as well as in recoil polarimetry (see, e.g., Ref. [1] for a recent review). Several spin observables with full angular coverage and fine energy binning are already available for πN, ηN, $\eta' N$, and KY final states.

Starting with the classical paper by Barker *et al.* [2], the question was intensively investigated as to which set of observables is necessary in order to reconstruct the helicity amplitudes in a model-independent way. Such an approach is called complete experiment analysis (CEA) and it turned out that a minimum of eight observables is necessary, including three types of polarization, beam, target, and recoil. However, even with modern data, such a CEA is at best possible

only in a very limited kinematic range. The general problem with the CEA is, however, that it does not directly lead to partial waves, since an angle-dependent overall phase remains unknown [3]. Therefore, the concept of a truncated partial-wave analysis (TPWA) has been extensively studied recently [4], where only partial waves up to an angular momentum of L_{max} are analyzed from the data, while all other higher partial waves are simply expected to be zero. Such TPWA analyses have been studied for kaon and pion photoproduction as well as for electroproduction [5,6]. It was shown that even a minimum set of four polarization observables are sufficient to extract all multipoles from numerical data, providing that the data are practically free of errors and do not contain higher partial-wave contributions. In practical analyses, however, the higher partial waves cannot be completely ignored and at least some next or next-to-next order needs to be included as a constraint. In charged pion photoproduction, the well-known pion-pole contribution gives such a constraint fairly model independently; for other channels such constraints have to be considered as model dependent. With such a TPWA analysis one also ends up with continuum phase ambiguity [7]; however, this phase is only energy dependent.

In the past, for pion photoproduction model-independent partial-wave analyses have been performed by using unitarity constraints. In the Δ region this has been done in an approach using Watson's theorem, where all multipole phases were fixed by unitarity to the well-known πN phases [8,9]. Near threshold, a PWA of π^0 photoproduction on the proton target became possible with unitarity constraints from charged pion photoproduction and well-known Born terms in the low-energy region [10].

At higher energies, starting with the excitation of the Roper resonance, such powerful constraints are no longer applica-

ble. However, analytical constraints from fixed-t dispersion relations can be applied to much higher energies [11–13], as long as the Mandelstam variable t remains in the region $-1.0 \text{ GeV}^2 \lesssim t < 0$.

In general, unitarity in a coupled channel formalism would allow us to constrain this phase. In the simplest case of pion photoproduction at low energies, this is provided by Watson's theorem. In other cases, this phase has to be fixed, e.g., to the phase of a reaction model. A detailed study of model-independent single-energy TPWAs was performed for the $\gamma p \rightarrow K^+ \Lambda$ reaction [14] using experimental data for eight observables as well as pseudodata generated from a model. In general, at each energy many different, experimentally indistinguishable, multipole solutions were obtained even if a global, energy-dependent phase was fixed. In order to obtain a solution, which is continuous in energy, the fit can be constrained to a parametrization of the amplitudes given by a preferred reaction model. This approach is commonly used in single-energy partial-wave analyses; however, it introduces a strong model dependence.

To avoid or at least reduce this model dependence significantly, we propose another method where continuity in energy is achieved by enforcing the full analyticity of the amplitudes not in one but in two Mandelstam variables. Amplitudes at different energies are not fully independent from each other but they are related by analyticity in Mandelstam s at a fixed value of the Mandelstam variable t. The main idea of the approach is to impose this analyticity in s at fixed values of t in addition to the analyticity in t at fixed energy. The method was fully developed and applied by Höhler in KH80 SE πN elastic PWA [15].

We apply our approach to the $\gamma p \rightarrow \eta p$ reaction in the energy range from threshold up to center-of-mass energies of $W = 1.85$ GeV. In this range, high-precision data of the differential cross section, as well as on photon beam (Σ), target (T), and beam-target (F) asymmetries in particular from MAMI [16–18] and GRAAL [19] are available. As the η meson is isoscalar, no isospin separation of the amplitudes is necessary.

Different reaction models for η photoproduction have been developed. First of all, they give an energy-dependent parametrization of the partial waves, and second, they can then be used for a (model-dependent) single-energy analysis. Isobar models introduce nucleon resonances with Breit-Wigner forms [11,20–23], T-matrix methods parametrize partial-wave amplitudes and search for resonances in the fitted solutions [24]. Coupled-channels approaches with K-matrix methods [25–27] and with meson-baryon dynamics [28] involve a series of hadronic channels, where experimental data have been measured. At higher energies, outside of the resonance region, Regge models have been successfully applied [21,29,30], and for an analytical connection between resonance and Regge regions, finite-energy sum rules have been investigated [31].

In parts of our studies, in particular for pseudodata simulations, the isobar model EtaMAID for η and η' photo and electroproduction on nucleons [20,21] has been applied. The model includes nucleon resonances in the s channel parameterized with Breit-Wigner shapes and nonresonant background.

Recently, three updated versions were published and will be addressed in our current work as I, II, and III. In version I, EtaMAID-2015 [32], the background consists of nucleon Born terms in the s and u channels and the ρ and ω meson exchange in the t channel with pole-like Feynman propagators. In version II, EtaMAID-2016 [33], the background from Born terms was excluded because of very small contribution. The background is described by vector and axial-vector meson exchanges in the t channel using the Regge cut phenomenology. Version III, EtaMAID-2017 [16], is very close to version II. In this version, a fit procedure was mainly improved and currently gives the best description of the experimental data.

The paper is organized as follows. In Sec. II, we will first give the basic formalism for kinematics, amplitudes, and observables. In Sec. III, we describe the method of imposing fixed-t analyticity to the partial-wave analysis in an iterative procedure. As a test of our procedure, in Sec. IV we perform an analytically constrained partial-wave analysis with input from pseudodata, generated from a recent version of the EtaMAID model. As a real data application, in Sec. V we analyze recent experimental data for η photoproduction. Finally, in Sec. VI we discuss our results and the remaining ambiguities due to limitations in the data base and residual model uncertainties and give an outlook for future developments.

II. FORMALISM

A. Kinematics in η photoproduction

For η photoproduction on the nucleon, we consider the reaction

$$\gamma(k) + N(p_i) \rightarrow \eta(q) + N'(p_f), \tag{1}$$

where the variables in brackets denote the four-momenta of the participating particles. These are $k^\mu = (k, \mathbf{k})$, $q^\mu = (\omega, \mathbf{q})$ for photon and η meson, and $p_i^\mu = (E_i, \mathbf{p}_i)$, $p_f^\mu = (E_f, \mathbf{p}_f)$ for incoming and outgoing nucleons, respectively. The familiar Mandelstam variables are given as

$$s = W^2 = (p_i + k)^2, \quad t = (q - k)^2, \quad u = (p_f - q)^2, \tag{2}$$

and the sum of the Mandelstam variables is given by the sum of the external masses

$$s + t + u = 2m_N^2 + m_\eta^2, \tag{3}$$

where m_N and m_η are masses of proton and η meson, respectively. In the η-nucleon center-of-mass (c.m.) system, we have $\mathbf{p}_i = -\mathbf{k}$, $\mathbf{p}_f = -\mathbf{q}$, and the energies and momenta can be related to the Mandelstam variable s by

$$k = |\mathbf{k}| = \frac{s - m_N^2}{2\sqrt{s}}, \quad \omega = \frac{s + m_\eta^2 - m_N^2}{2\sqrt{s}}, \tag{4}$$

$$q = |\mathbf{q}| = \left[\left(\frac{s - m_\eta^2 + m_N^2}{2\sqrt{s}} \right) - m_N^2 \right]^{\frac{1}{2}}, \tag{5}$$

$$E_i = \frac{s - m_N^2}{2\sqrt{s}}, \quad E_f = \frac{s + m_N^2 + m_\eta^2}{2\sqrt{s}}, \tag{6}$$

$W = \sqrt{s}$ is the c.m. energy. Furthermore, we will also refer to the laboratory energy of the photon, $E = (s - m_N^2)/(2m_N)$.

Starting from the s-channel reaction $\gamma + N \Rightarrow \eta + N$, using crossing relation, one obtains two other channels:

$$\gamma + \eta \;\Rightarrow\; N + \bar{N} \qquad t - \text{channel}, \tag{7}$$

$$\eta + \bar{N} \;\Rightarrow\; \gamma + \bar{N} \qquad u - \text{channel}. \tag{8}$$

All three channels defined above are described by a set of four invariant amplitudes. The singularities of the invariant amplitudes are defined by unitarity in s, u, and t channels:

$$s\text{-channel cut:} \;(m_N + m_\eta)^2 \leqslant s < \infty, \tag{9}$$

$$\text{with unphysical cut:} \;(m_\pi + m_N)^2 \leqslant s \leqslant (m_\eta + m_N)^2, \tag{10}$$

$$u\text{-channel cut:} \;(m_N + m_\eta)^2 \leqslant u < \infty, \tag{11}$$

$$\text{with unphysical cut:} \;(m_\pi + m_N)^2 \leqslant u \leqslant (m_\eta + m_N)^2, \tag{12}$$

and nucleon poles at $s = m_N^2$, $u = m_N^2$. The crossing symmetrical variable is

$$\nu = \frac{s - u}{4m_N}. \tag{13}$$

The s-channel region is shown in Fig. 1. The upper and lower boundaries of the physical region are given by the scattering angles $\theta = 0$ and $\theta = 180°$, respectively. The horizontal
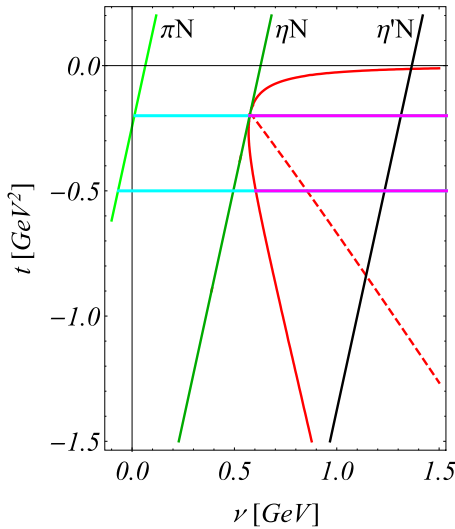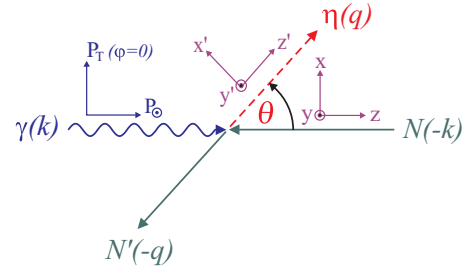

FIG. 2. Kinematics of photoproduction and frames for polarization. The frame $\{x,y,z\}$ is used for target polarization $\{P_x, P_y, P_z\}$, whereas the recoil polarization $\{P_{x'}, P_{y'}, P_{z'}\}$ is defined in the frame $\{x',y',z'\}$, which is rotated around $y' = y$ by the polar angle θ. The azimuthal angle φ is defined in the $\{x,y\}$ plane and is zero in the projection shown in the figure.

lines at $t = -0.2$ and $-0.5\,\text{GeV}^2$ show the kinematical regions, where our fixed-t analyses will be discussed in detail. The c.m. energy W and the c.m. scattering angle θ can be obtained from the variables ν and t by

$$W^2 = m_N(m_N + 2\nu) - \tfrac{1}{2}\big(t - m_\eta^2\big) \tag{14}$$

and

$$\cos\theta = \frac{t - m_\eta^2 + 2\,k\,\omega}{2\,k\,q}. \tag{15}$$

B. Cross section and polarization observables

Experiments with three types of polarization can be performed in meson photoproduction: photon beam polarization, polarization of the target nucleon, and polarization of the recoil nucleon. Target polarization will be described in the frame $\{x,y,z\}$ in Fig. 2, with the z axis pointing into the direction of the photon momentum $\hat{\mathbf{k}}$, the y axis perpendicular to the reaction plane, $\hat{\mathbf{y}} = \hat{\mathbf{k}} \times \hat{\mathbf{q}}/\sin\theta$, and the x axis given by $\hat{\mathbf{x}} = \hat{\mathbf{y}} \times \hat{\mathbf{z}}$. For recoil polarization we will use the frame $\{x',y',z'\}$, with the z' axis defined by the momentum vector of the outgoing meson $\hat{\mathbf{q}}$, the y' axis as for target polarization, and the x' axis given by $\hat{\mathbf{x}}' = \hat{\mathbf{y}}' \times \hat{\mathbf{z}}'$.

The photon polarization can be linear or circular. For a linear photon polarization ($P_T = 1$) in the reaction plane $\hat{\mathbf{x}}$, we get $\varphi = 0$ and perpendicular, in direction $\hat{\mathbf{y}}$, the polarization angle is $\varphi = \pi/2$. For right-handed circular polarization $P_\odot = +1$.

We may classify the differential cross sections by the three classes of double polarization experiments and one class of triple polarization experiments, which, however, do not give additional information:

(1) polarized photons and polarized target

$$\begin{aligned}
\frac{d\sigma}{d\Omega} = \sigma_0 \{ & 1 - P_T \Sigma \cos 2\varphi \\
& + P_x(-P_T H \sin 2\varphi + P_\odot F) \\
& + P_y(T - P_T P \cos 2\varphi) \\
& + P_z(P_T G \sin 2\varphi - P_\odot E)\},
\end{aligned} \tag{16}$$

FIG. 1. The Mandelstam plane for η photoproduction on the nucleon. The red solid curves are the boundaries of the physical region from $\theta = 0$ to $\theta = 180°$ and the red dashed line shows $\theta = 90°$. The tilted vertical lines from left to right are the thresholds for $\pi N, \eta N, \eta' N$ production, respectively. The (blue) dotted line shows the u-channel threshold $u = (m_N + m_\pi)^2$. The horizontal lines denote the t values $-0.2, -0.5\,\text{GeV}^2$, where we will show our fixed-t analyses. The magenta parts give the part inside the physical region, where the cyan parts have to be evaluated in the unphysical region. The threshold values for γ, η in W are $W_{\text{thr}} = 1.486$ GeV ($t = -0.2$ GeV^2) and $W_{\text{thr}} = 1.554$ GeV ($t = -0.5$ GeV^2).

(2) polarized photons and recoil polarization

$$
\frac{d\sigma}{d\Omega} = \sigma_0\{1 - P_T \Sigma \cos 2\varphi
$$
$$
+ P_{x'}(-P_T O_{x'} \sin 2\varphi - P_\odot C_{x'})
$$
$$
+ P_{y'}(P - P_T T \cos 2\varphi)
$$
$$
+ P_{z'}(-P_T O_{z'} \sin 2\varphi - P_\odot C_{z'})\}, \quad (17)
$$

(3) polarized target and recoil polarization

$$
\frac{d\sigma}{d\Omega} = \sigma_0\{1 + P_y T + P_{y'} P + P_{x'}(P_x T_{x'} - P_z L_{x'})
$$
$$
+ P_{y'} P_y \Sigma + P_{z'}(P_x T_{z'} + P_z L_{z'})\}. \quad (18)
$$

In these equations, σ_0 denotes the unpolarized differential cross section, the transverse degree of photon polarization is denoted by P_T, $P_\odot$ is the right-handed circular photon polarization, and φ is the azimuthal angle of the photon polarization vector in respect to the reaction plane. Instead of asymmetries, in the following we will often discuss the product of the unpolarized cross section with the asymmetries and will use the notation $\check{\Sigma} = \sigma_0 \Sigma, \check{T} = \sigma_0 T, \ldots$. In the appendix, we give expressions of the observables in terms of Chew-Goldberger-Low-Nambu (CGLN) and helicity amplitudes.

C. Invariant amplitudes and fixed-t dispersion relations

The nucleon electromagnetic current for pseudoscalar meson photoproduction can be expressed in terms of four invariant amplitudes A_i [34],

$$
J^\mu = \sum_{i=1}^{4} A_i(\nu,t) M_i^\mu, \quad (19)
$$

with the gauge-invariant four-vectors M_i^μ given by

$$
M_1^\mu = -\frac{1}{2} i \gamma_5 (\gamma^\mu \slashed{k} - \slashed{k} \gamma^\mu),
$$
$$
M_2^\mu = 2i\gamma_5 \left[P^\mu k \cdot \left(q - \frac{1}{2}k\right) - \left(q - \frac{1}{2}k\right)^\mu k \cdot P \right],
$$
$$
M_3^\mu = -i\gamma_5(\gamma^\mu k \cdot q - \slashed{k} q^\mu),
$$
$$
M_4^\mu = -2i\gamma_5(\gamma^\mu k \cdot P - \slashed{k} P^\mu) - 2m_N M_1^\mu, \quad (20)
$$

where $P^\mu = (p_i^\mu + p_f^\mu)/2$ and the γ matrices are defined as in Ref. [35].

Invariant amplitudes have definite crossing symmetry. For π^0 and η photoproduction, the amplitudes $A_{1,2,4}$ are crossing even and A_3 is crossing odd. In the work of Aznauryan [11,12] on pion and η photoproduction, a complete set of eight invariant amplitudes $B_i(\nu,t)$ and Dirac operators N_i^μ are introduced, allowing any arbitrary current to be expanded in this set of amplitudes:

$$
J^\mu = \sum_{i=1}^{8} B_i(\nu,t) N_i^\mu. \quad (21)
$$

If current conservation is implied, the eight amplitudes are reduced to six amplitudes in electroproduction. In photoproduction, the set of amplitudes is further reduced to four amplitudes, e.g., B_1, B_2, B_6, B_8 [12], which are then simple linear combinations of the four $A_i(\nu,t)$ amplitudes A_1, A_2, A_3, A_4:

$$
B_1(\nu,t) = A_1(\nu,t) - 2m_N A_4(\nu,t),
$$
$$
B_2(\nu,t) = \frac{1}{2}(t - \mu^2)A_2(\nu,t),
$$
$$
B_6(\nu,t) = -2A_4(\nu,t),
$$
$$
B_8(\nu,t) = -A_3(\nu,t). \quad (22)
$$

For the set of crossing symmetric amplitudes, $B = \{B_1, B_2, B_6, B_8/\nu\}$, fixed-$t$ dispersion relations can be written in the following form:

$$
\mathrm{Re}\,B(\nu,t) = B^N(\nu,t) + \frac{2}{\pi} \mathcal{P} \int_{\nu_{\mathrm{thr}}}^{\infty} d\nu' \frac{\nu' \,\mathrm{Im}\,B(\nu',t)}{\nu'^2 - \nu^2}, \quad (23)
$$

where B^N is the nucleon pole contribution that can be calculated from the Born terms in pseudoscalar coupling, and ν_{thr} corresponds to the πN photoproduction threshold. The nucleon pole terms B_i^N for γ, η are given by

$$
B_1^N(\nu,t) = \frac{e\,g_{\eta N}(1 + \kappa_N)}{m_N} \frac{\nu_B}{\nu^2 - \nu_B^2},
$$
$$
B_2^N(\nu,t) = \frac{-e\,g_{\eta N}}{m_N} \frac{\nu_B}{\nu^2 - \nu_B^2},
$$
$$
B_6^N(\nu,t) = \frac{e\,g_{\eta N}\kappa_N}{m_N^2} \frac{\nu_B}{\nu^2 - \nu_B^2},
$$
$$
B_8^N(\nu,t) = \frac{e\,g_{\eta N}\kappa_N}{2m_N^2} \frac{\nu}{\nu^2 - \nu_B^2}, \quad (24)
$$

where e and $g_{\eta N} = 0.112$ are the electromagnetic and hadronic coupling constants, κ_N is the anomalous magnetic moment of the nucleon, and $\nu_B = (t - m_\eta^2)/4m_N$.

D. CGLN and helicity amplitudes

For PWA, the CGLN amplitudes $F_i(E,x)$ [36] are conveniently used. They are defined in the center of mass frame using Coulomb gauge. The matrix element $\mathcal{F}$ with the electromagnetic current of Eq. (19) then reads

$$
\mathcal{F} = -\epsilon_\mu J^\mu
$$
$$
= i\,(\vec{\sigma} \cdot \hat{\epsilon})\,F_1 + (\vec{\sigma} \cdot \hat{q})(\vec{\sigma} \times \hat{k}) \cdot \hat{\epsilon}\,F_2 + i\,(\hat{\epsilon} \cdot \hat{q})(\vec{\sigma} \cdot \hat{k})F_3
$$
$$
+ i(\hat{\epsilon} \cdot \hat{q})(\vec{\sigma} \cdot \hat{q})\,F_4, \quad (25)
$$

where $\epsilon^\mu = (0, \vec{\epsilon})$ and $\vec{\epsilon} \cdot \vec{k} = 0$. In partial-wave analysis of pseudoscalar meson photoproduction, it is convenient to work with CGLN amplitudes giving simple representations in terms of electric and magnetic multipoles and derivatives of Legendre polynomials

$$
F_1 = \sum_{l=0}^{\infty} \{(lM_{l+} + E_{l+})P'_{l+1}(x)
$$
$$
+ [(l + 1)M_{l+} + E_{l-}]P'_{l-1}(x)\},
$$
$$
F_2 = \sum_{l=1}^{\infty} [(l + 1)M_{l+} + lM_{l-}]P'_l(x),
$$

$$F_3 = \sum_{l=1}^{\infty}[(E_{l+} - M_{l+})P''_{l+1} + (E_{l-} + M_{l-})P''_{l-1}(x)],$$

$$F_4 = \sum_{l=2}^{\infty}[M_{l+} - E_{l+} - M_{l-} - E_{l-}]P''_l(x), \qquad (26)$$

where $x = \cos\theta$ is the cosine of the scattering angle. Another common set of amplitudes, which we will use in our current work, are helicity amplitudes, linearly related to the CGLN amplitudes by

$$H_1 = -\frac{1}{\sqrt{2}}\sin\theta\cos\frac{\theta}{2}(F_3 + F_4),$$

$$H_2 = \sqrt{2}\cos\frac{\theta}{2}\left[(F_2 - F_1) + \frac{1 - \cos\theta}{2}(F_3 - F_4)\right],$$

$$H_3 = \frac{1}{\sqrt{2}}\sin\theta\sin\frac{\theta}{2}(F_3 - F_4),$$

$$H_4 = \sqrt{2}\sin\frac{\theta}{2}\left[(F_1 + F_2) + \frac{1 + \cos\theta}{2}(F_3 + F_4)\right]. \quad (27)$$

III. IMPOSING FIXED-t ANALYTICITY

This is the central part of our paper. Partly, it contains lost knowledge in partial-wave analysis of scattering data.

A. Pietarinen's expansion method

To introduce our method, we follow Pietarinen's papers [37–39] and the review by Hamilton and Petersen [40] and consider scattering amplitude having a simple analytic structure at a fixed-t in the complex ν plane:

  (i) $F(\nu)$ is analytic function having a cut from ν_{th} to ∞.
 (ii) $F(\nu)$ is bounded in the ν plane.

In addition, we suppose that $F(\nu)$ obeys Schwarz reflection principle $F(\nu^*) = F^*(\nu)$. In most problems, only information on $|F(\nu)|^2$ or some other bilinear form are available, but, for simplicity of the description of the method, let us suppose that we have the following information on the amplitude $F(\nu)$:

  (a)   Real parts $\mathrm{Re}F(\nu_1)$, …, $\mathrm{Re}F(\nu_M)$ at M points ν_1, …, ν_M with errors $\varepsilon_1, \ldots, \varepsilon_M$.
  (b)   Imaginary parts $\mathrm{Im}F(\nu_{M+1})$, …, $\mathrm{Im}F(\nu_{M+N})$ at N points $\nu_{M+1}, \ldots, \nu_{M+N}$ with errors $\varepsilon_{M+1}, \ldots, \varepsilon_{M+N}$.

The task is to find an approximant $\varphi(\nu)$ of the function $F(\nu)$ having the same analytic structure. The standard procedure is to find a minimum of the quadratic form

$$\chi^2(\varphi) = \sum_{i=1}^{M}\left(\frac{\mathrm{Re}\varphi(\nu_i) - \mathrm{Re}F(\nu_i)}{\varepsilon_i}\right)^2$$

$$+ \sum_{i=M+1}^{N+M}\left(\frac{\mathrm{Im}\varphi(\nu_i) - \mathrm{Im}F(\nu_i)}{\varepsilon_i}\right)^2. \quad (28)$$

There are many approximants giving very small χ^2. Most of them are nonsmooth inside or outside of the region where the data on $F(\nu)$ are available. The problem to find an optimal one

consists of finding a compromise between a good fit to the data and the smoothness of the approximant. The standard approach is to introduce a penalty function $\Phi(\varphi)$ (also known as a convergence test function), which makes a choice of the smoothest approximant that has an acceptable χ^2. Such an approximant is obtained by finding a minimum of the quadratic form

$$X^2 = \chi^2(\varphi) + \Phi(\varphi), \qquad (29)$$

where $\chi^2(\varphi)$ is defined by Eq. (28). The form of the penalty function $\Phi(\varphi)$ is not unique. To find $\Phi(\varphi)$, Pietarinen [37] proceeded as follows:

  (1)   Conformal mapping

$$z = \frac{\alpha - \sqrt{\nu_{th} - \nu}}{\alpha + \sqrt{\nu_{th} - \nu}}, \quad \alpha \in \mathbb{R}, \alpha > 0, \qquad (30)$$

     transforms a complex ν plane with physical cut along $\nu_{th} \leqslant \nu < \infty$ into unit circle $|z| = 1$. The physical cut is mapped on $|z| = 1$.
  (2)   Any function having properties (i) and (ii) may be represented in the complex z plane by a convergent series

$$\varphi(z) = \sum_{n=0}^{\infty} c_n z^n, \qquad (31)$$

     which preserves the analytic properties of the approximant φ in the ν plane. As a consequence of real analyticity of the amplitude $F(\nu)$, the coefficients c_n are real.

The choice of the penalty function is not unique. Recently, popularity has gained for The least absolute shrinkage and selection operator (LASSO) method [41], in which the penalty function has the form

$$\Phi_{\mathrm{LASSO}} = \lambda \sum_{n=0}^{N_{\max}} |c_n|, \qquad (32)$$

where λ is a strength parameter and c_n are fitting parameters. Using arguments from complex analysis (theory of functions) and probability theory, Pietarinen found a penalty function for the approximant (31) in the form

$$\Phi(\varphi) = \lambda \sum_{n=0}^{\infty} (n+1)^3 c_n^2, \qquad (33)$$

where λ is a real scaling parameter (weight factor). It can be shown that higher coefficients c_n in expansion (33) are suppressed and behave as

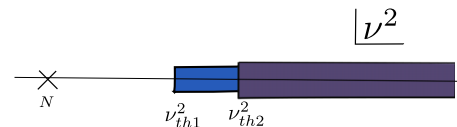$$|c_i| \leqslant \frac{1}{n^{\frac{3}{2}}\lambda}. \qquad (34)$$

FIG. 3. Analytic structure of invariant amplitudes for a fixed-t value in the complex ν^2 plane.
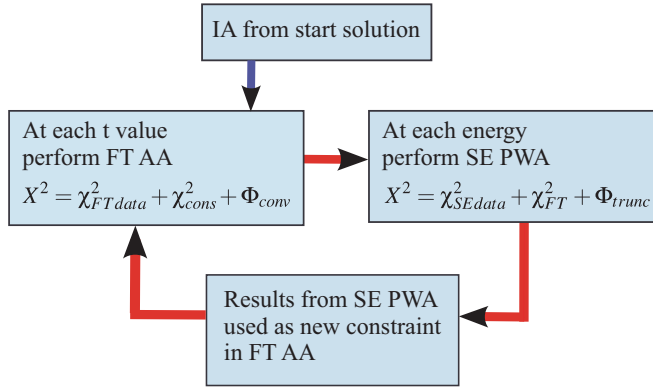
FIG. 4. Iterative minimization scheme which achieves point-to-point continuity in energy using fixed-t analyticity as a constraint. (IA, invariant amplitudes; FT AA, fixed-t amplitude analysis; SE PWA, single-energy partial wave analysis).

Therefore, expansion (31) may be truncated at some finite order N_{max}. With the approximant in the form (31) and penalty function Φ in the form (33), the minimization of X^2 is a compromise between fitting the data and keeping higher coefficients in (31) small. With finite numbers of coefficients in expansion (31) and data on $F(\nu)$ as described in (a) and (b) in subsection A, the minimization of X^2 consists of solving

a system of N_{max} linear equations, which may be performed quickly and reliably. Following Höhler [15] (Appendix A6.3.4, p. 536), the representation (31) with penalty (33) is called Pietarinen's expansion and the method is called Pietarinen's expansion method. As concluding remarks concerning Pietarinen's expansion, we want to point out the following:

(1) Due to conformal mapping in the form (30), a polynomial expansion of any order $n \geqslant 1$ reconstructs the analytic structure of the amplitude at a fixed value of t, i.e., fixed-t analyticity.
(2) The conformal variable z can be defined in such a way to assure the correct crossing property of the scattering amplitudes.
(3) The asymptotical behavior of the amplitudes can be imposed explicitly.
(4) Technically, the expansion (31) can be evaluated quickly and reliably using nested multiplication.

Because of the bilinear structure of the relations between observables and invariant amplitudes, the minimization of X^2 becomes nonlinear and therefore much more demanding. Observables are expressed in terms of several amplitudes (depending on spin and isospin structure of the particular process). Each of the amplitudes is represented by its own representation (31) and all coefficients are to be determined simultaneously. According to Pietarinen, one has to minimize
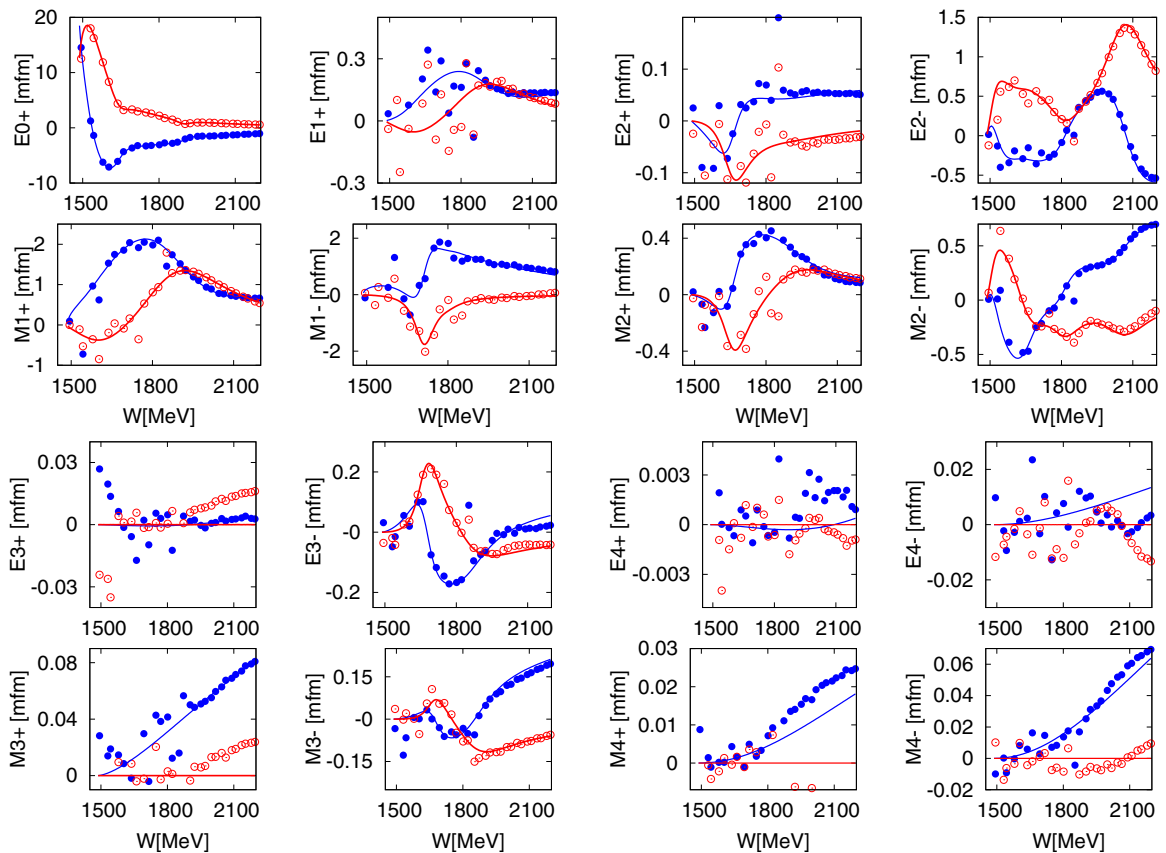

FIG. 5. Result of unconstrained single-energy fit described in the text. The blue and red points show the real and imaginary parts of the multipoles obtained in the fit compared to the "true" multipoles from the underlying EtaMAID-2015 model (blue and red solid lines).

a quadratic form

$$X^2 = \chi^2_{\text{data}} + \Phi, \tag{35}$$

where the penalty function Φ consists of a sum of forms (33), one for each amplitude.

B. Representation of invariant amplitudes in η photoproduction fixed-t amplitude analysis

As stated above, η photoproduction can be described by four independent, crossing symmetric amplitudes B_1, B_2, B_6, and B_8/ν. Their analytic structure for fixed-t values (fixed-t analyticity) in the complex ν^2 plane is shown in Fig. 3. The values ν_{th1} and ν_{th2} correspond to the thresholds of πp ($W_{\pi,\text{th}} = 1.077$ GeV) and ηp ($W_{\eta,\text{th}} = 1.486$ GeV), respectively. N is the nucleon pole. To represent an analytic function having two branch points and two corresponding cuts, we use two conformal mappings,

$$z_1 = \frac{\alpha_1 - \sqrt{\nu_{\text{th1}}^2 - \nu^2}}{\alpha_1 + \sqrt{\nu_{\text{th1}}^2 - \nu^2}}, \quad z_2 = \frac{\alpha_2 - \sqrt{\nu_{\text{th2}}^2 - \nu^2}}{\alpha_2 + \sqrt{\nu_{\text{th2}}^2 - \nu^2}}, \tag{36}$$

where α_1, α_2 are real positive parameters. First, z_1 maps the ν^2 plane into the unit circle $|z_1| \leqslant 1$. Values on the physical cut ($\nu_{\text{th1}}^2, \infty$) are mapped onto the unit circle $|z_1| = 1$. Second, z_2 maps the values on the physical cut ($\nu_{\text{th2}}^2, \infty$) onto the unit circle $|z_2| = 1$. The invariant amplitudes are represented by two Pietarinen expansions

$$\overline{B}_1 = B_1 - B_1^N = (1 + z_1) \sum_i b_{1i}^{(1)} z_1^i + (1 + z_2) \sum_i b_{1i}^{(2)} z_2^i,$$

$$\overline{B}_2 = B_2 - B_2^N = (1 + z_1) \sum_i b_{2i}^{(1)} z_1^i + (1 + z_2) \sum_i b_{2i}^{(2)} z_2^i,$$

$$\overline{B}_6 = B_6 - B_6^N = (1 + z_1) \sum_i b_{6i}^{(1)} z_1^i + (1 + z_2) \sum_i b_{6i}^{(2)} z_2^i,$$

$$\frac{\overline{B}_8}{\nu} = \frac{B_8}{\nu} - \frac{B_8^N}{\nu} = (1 + z_1) \sum_i b_{8i}^{(1)} z_1^i + (1 + z_2) \sum_i b_{8i}^{(2)} z_2^i, \tag{37}$$

where B_i^N are the nucleon pole contributions. The factors $(1 + z_1)$ and $(1 + z_2)$ in front of the corresponding power series assure that the amplitudes B_i go to zero at infinity. By construction, the expansions (37) represent crossing even amplitudes,
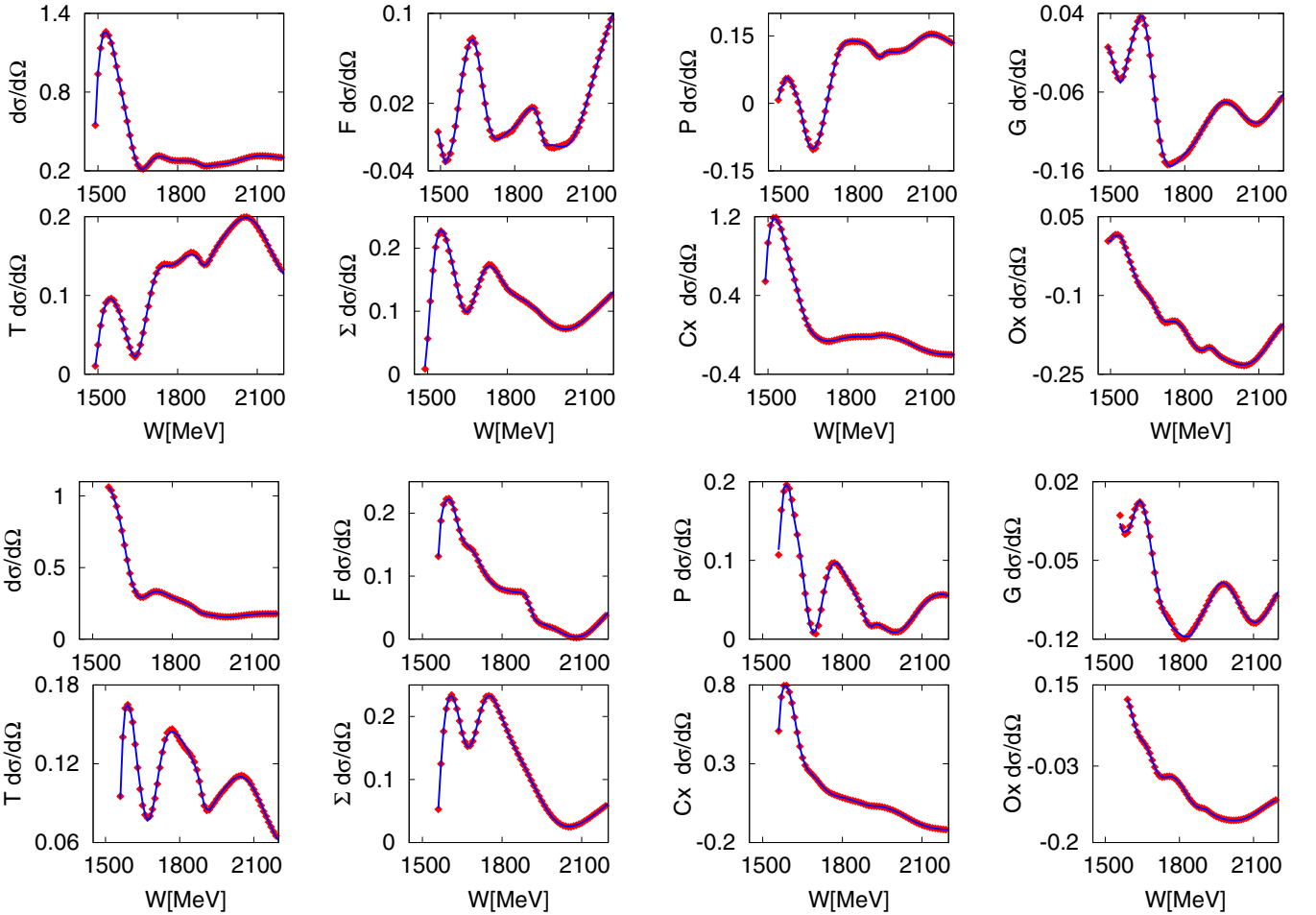

FIG. 6. Fixed-t amplitude analysis of a complete set of pseudodata at $t = -0.2\,\text{GeV}^2$ (top) and $t = -0.5\,\text{GeV}^2$ (bottom). The minimization is performed according to Eq. (47). The data points are pseudodata with a precision of 0.1%. The lines are obtained from the Pietarinen expansion with fitted coefficients.
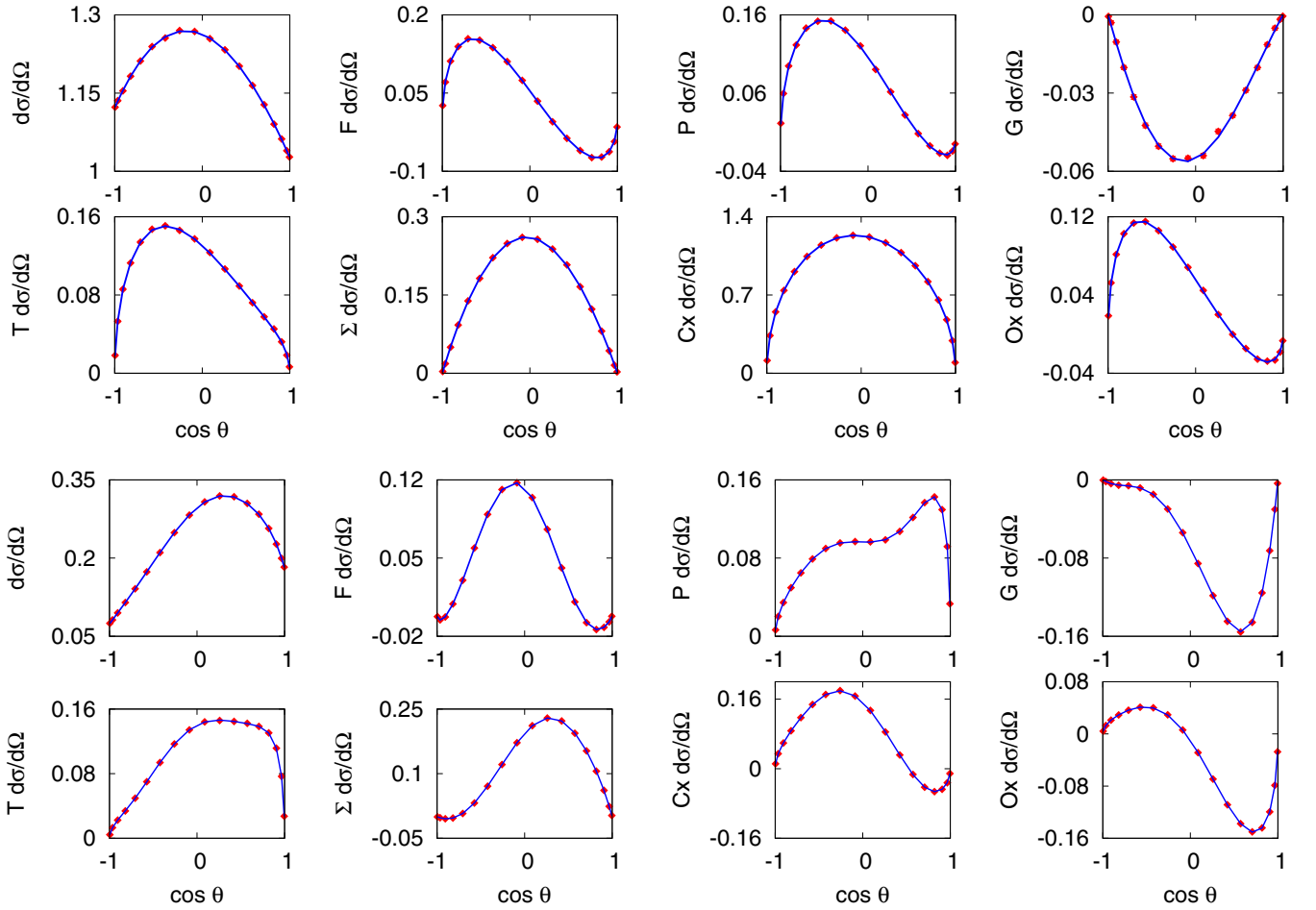
FIG. 7. Single-energy partial-wave analysis of a complete set of pseudodata at $W = 1543$ MeV (top) and $W = 1770$ MeV (bottom). The minimization is performed according to Eq. (49). The data points are pseudodata with a precision of 0.1%. The lines are obtained from the CGLN amplitudes with fitted multipoles up to $L_{\max} = 5$.

having analytic structure required by the fixed-t analyticity from Mandelstam hypothesis applied to η photoproduction. The coefficients in (37) are obtained by fitting the quadratic form

$$X^2 = \chi^2_{\text{FTdata}} + \Phi_{\text{conv}} \tag{38}$$
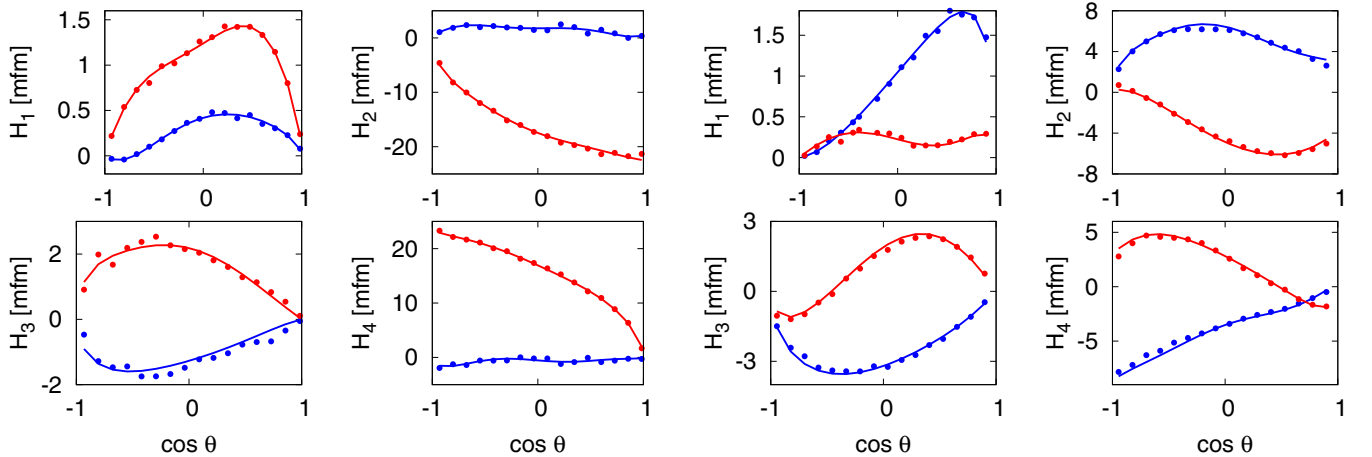

FIG. 8. Helicity amplitudes $H_k(W, \cos\theta)$ after final (second) iteration at $W = 1543$ MeV (left) and $W = 1660$ MeV (right). Real and imaginary parts of the helicity amplitudes (blue and red dots) are obtained from independent fixed-t AA at different t values in previous (first) iteration. The full lines are the helicity amplitudes from final iteration in SE PWA.
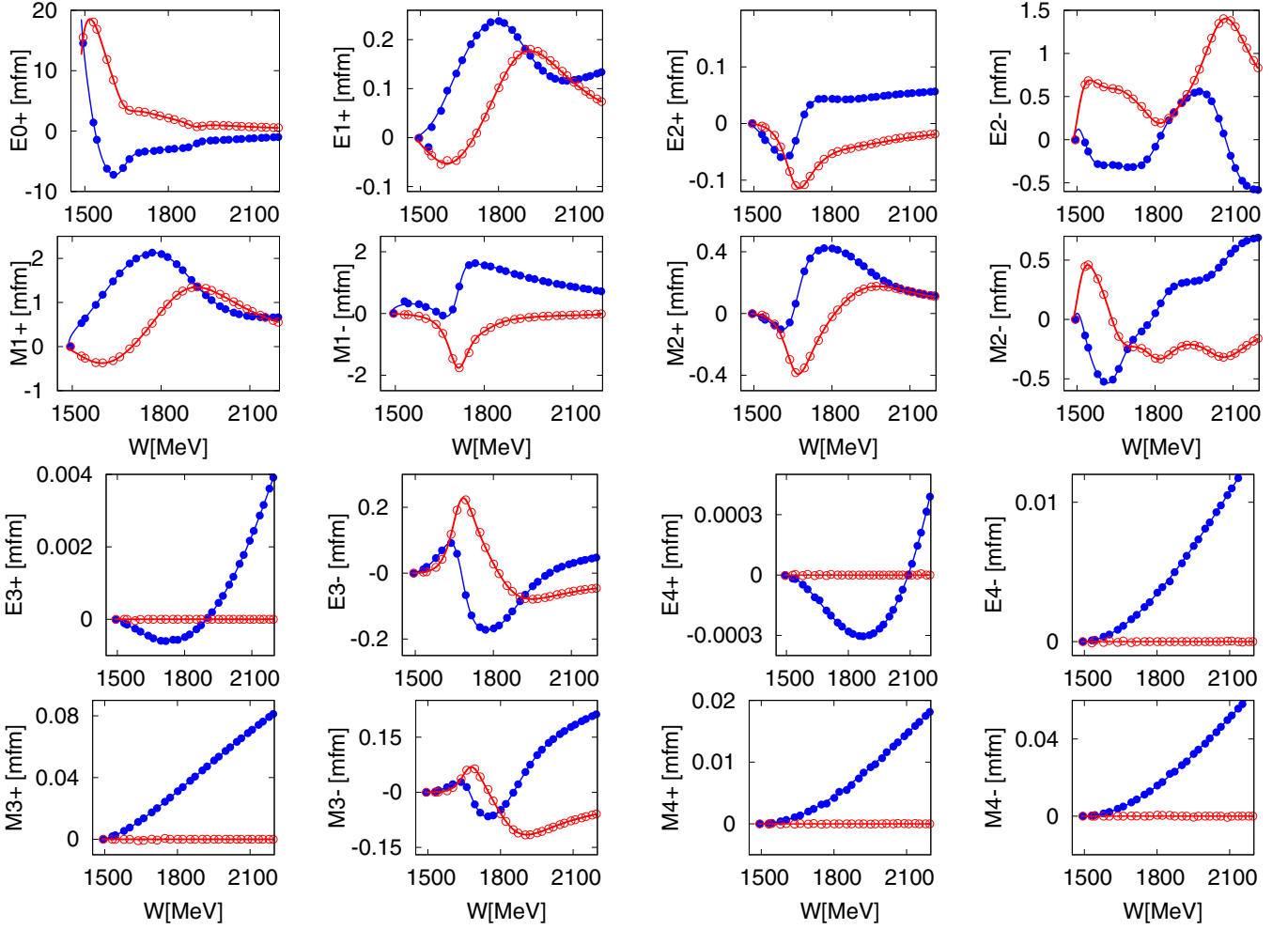
FIG. 9. Real (blue) and imaginary (red) parts of electric and magnetic multipoles up to $L = 4$. The points are the result of the analytically constrained single-energy fit to the pseudodata and are compared to the multipoles of the underlying EtaMAID-2015 model, shown as solid lines.

to the fixed-t data with χ^2_{FTdata} in the form

$$\chi^2_{\text{FTdata}} = \sum_{a=1}^{N^O} \sum_{n=1}^{N^E} \left[\frac{O_a(s_n,t)^{\exp} - O_a(s_n,t)^{\text{fit}}}{\Delta O_a(s_n,t)^{\exp}} \right]^2, \quad (39)$$

where N^O is number of observables, $O_a = \{\sigma_0, \check{\Sigma}, \check{T}, \check{F}, ...\}$ with corresponding errors ΔO_a.

Φ_{conv} is a Pietarinen's convergence test function [15,38] (Chapter 2.1.7, page 405 in Ref. [15]),

$$\Phi_{\text{conv}} = \Phi_1 + \Phi_2 + \Phi_6 + \Phi_8, \quad (40)$$

$$\Phi_k = \lambda_{k1} \sum_{i=0}^{N_1} \left(b_{ki}^{(1)}\right)^2 (i+1)^3 + \lambda_{k2} \sum_{i=0}^{N_2} \left(b_{ki}^{(2)}\right)^2 (i+1)^3, \quad (41)$$

where $\lambda_{k1}, \lambda_{k2}$ are adjustable weight parameters with $k = 1, 2, 6, 8$. The procedure described above is known as a fixed-t amplitude analysis (FT AA). For a given t value, the result is a set of coefficients $\{b_{ki}^{(1)}\}$, $\{b_{ki}^{(2)}\}$, with $k = 1, 2, 6, 8$. Invariant and helicity amplitudes at predetermined t values may be

calculated at any energy W and any scattering angle inside the physical region using the formula

$$\cos\theta_i = \frac{t_i - m_\eta^2 + 2k\omega}{2kq}, \quad |\cos\theta_i| \leqslant 1, \quad t_i \in [t_{\min}, t_{\max}]. \quad (42)$$

C. Single-energy partial-wave analysis

In single-energy partial-wave analysis (SE PWA) we minimize the quadratic form

$$X^2 = \chi^2_{\text{SEdata}} + \Phi_{\text{trunc}}. \quad (43)$$

χ^2_{SEdata} contains all experimental data at a given energy W

$$\chi^2_{\text{SEdata}} = \sum_{a=1}^{N^O} \sum_{i=1}^{N^D} \left[\frac{O_a(\theta_i)^{\exp} - O_a(\theta_i)^{\text{fit}}}{\Delta O_a(\theta_i)^{\exp}} \right]^2. \quad (44)$$

As before, N^O is the number of observables, N^D is corresponding number of data for observable O_a, and $O_a(\theta_i)^{\exp}$ are experimental values of observable O_a with corresponding errors $\Delta O_a(\theta_i)$. $O_a(\theta_i)^{\text{fit}}$ are values of the observable
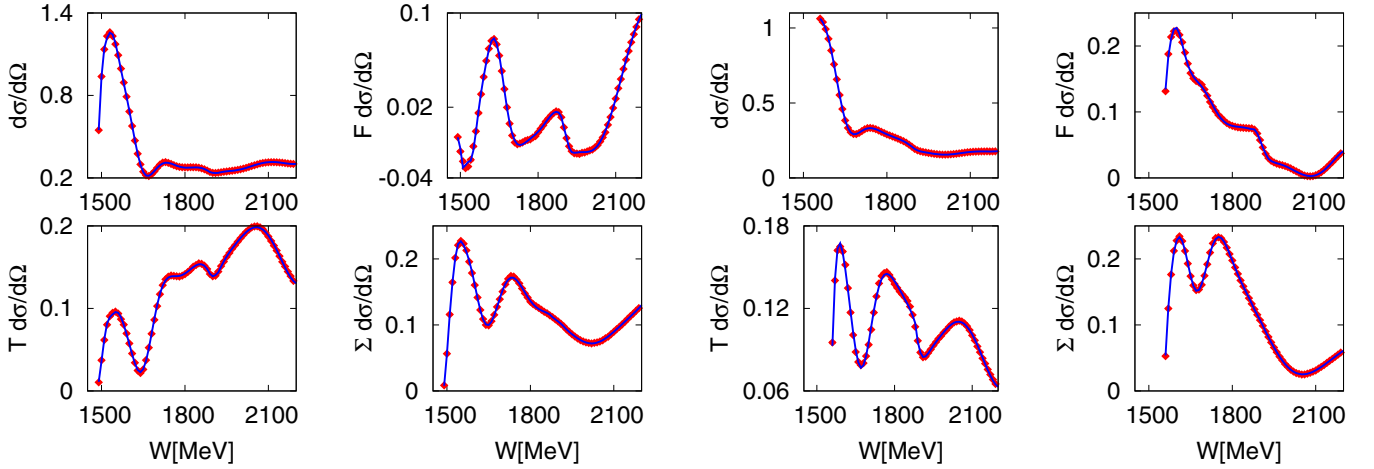
FIG. 10. Fixed-*t* amplitude analysis of four observables of pseudodata at $t = -0.2\,\text{GeV}^2$ (left) and $t = -0.5\,\text{GeV}^2$ (right). The data points are pseudodata with a precision of 0.1%. The lines are obtained from the Pietarinen expansion with fitted coefficients.

O_a, evaluated from partial waves obtained in the fit. Φ_{trunc} makes a soft cutoff of higher partial waves and is effective at low energies close to threshold [15]. It is given by the formula

$$\Phi_{\text{trunc}} = \lambda_{\text{trunc}} \sum_{\ell=0}^{\ell_{\max}} \left[(\text{Re}\,T_{\ell\pm})^2 R_1^{2\ell} + (\text{Im}\,T_{\ell\pm})^2 R_2^{2\ell} \right]. \quad (45)$$

The form of Φ_{trunc} arises from the general behavior of partial waves as a function of angular momentum ℓ. For a given energy, the partial-wave expansion of invariant amplitudes converges in an ellipse in the $\cos\theta$ plane having foci at ± 1 and semiaxes y_0 and $\sqrt{y_0^2 - 1}$, where y_0, different for real and imaginary parts, is determined by the nearest double spectral region [15,42]. For the simplest, spinless case [40], the partial wave expansion converges if higher partial waves $T_{l\pm}(l \gg 1)$

behave like

$$(\text{Im}\,T_{\ell\pm})^2 \leqslant C R_1^{-2\ell}, \quad (46)$$

where $R_1 = y_0 + \sqrt{y_0^2 - 1}$. A similar inequality holds for the real part with corresponding value of R_2. This result justifies the use of finite Legendre series in fitting scattering data. In η photoproduction, due to the unphysical cut in the t channel starting at $t = 4m_\pi^2$, the edge of the double spectral region approaches $t = 4m_\pi^2$ as s goes to infinity. We make a simple choice: $y_0 = \cos[\theta(t = 4m_\pi^2)]$, $|y_0| > 1$ for both real and imaginary parts (i.e., $R_1 = R_2 = R = y_0 + \sqrt{y_0^2 - 1} > 1$). In addition, we assume that electric and magnetic multipoles behave roughly in the same way. In order to get small values of χ^2, the minimizer has to keep Φ_{trunc} small, imposing small values of higher multipoles. As mentioned, Φ_{trunc} is effective at low energies and makes a soft cutoff of higher multipoles.
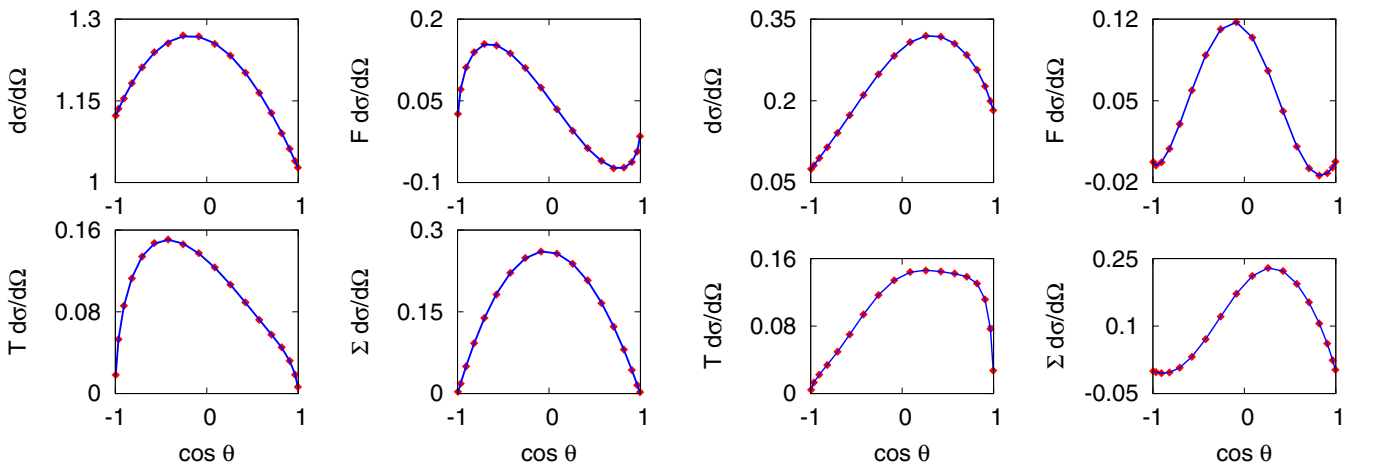

FIG. 11. Single-energy partial wave analysis of a set with four observables of pseudodata at $W = 1543$ MeV (left) and $W = 1770$ MeV (right). The data points are pseudodata with a precision of 0.1%. The lines are the results of the fixed-*t* constrained single-energy fit describes in the text.
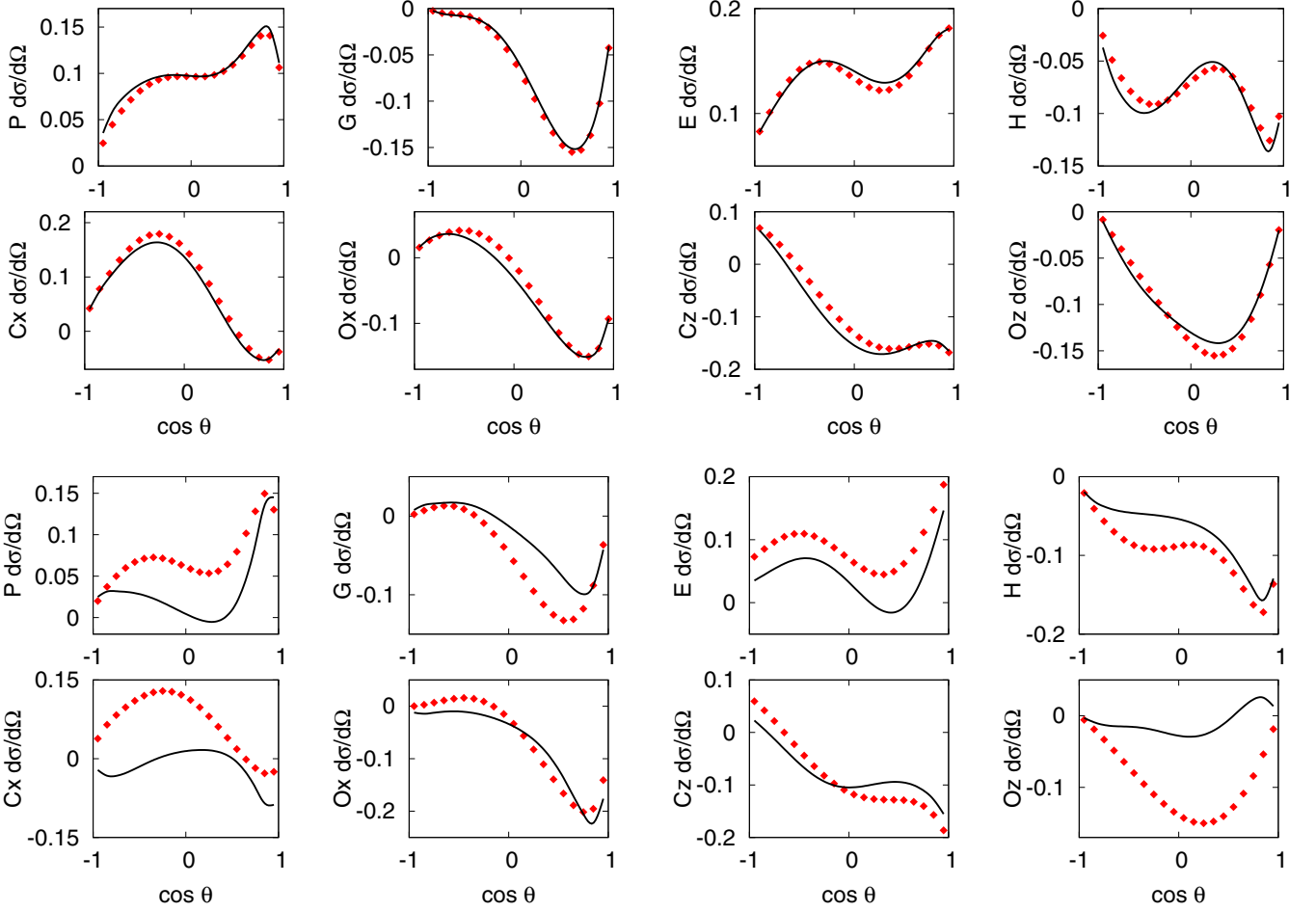
FIG. 12. Predictions for polarization observables from groups of type $\mathcal{S}, \mathcal{BT}$, and $\mathcal{BR}$ that are not fitted; shown at $W = 1770$ MeV (top) and $W = 1900$ MeV (bottom). The data points are pseudodata with a precision of 0.1% (red points). The lines are obtained in the fit with four observables $\sigma_0, \check{\Sigma}, \check{T}$, and $\check{F}$, from the CGLN amplitudes with fitted multipoles up to $L_{\max} = 5$.

D. Iterative minimization scheme

The method consists of two separate analyses, the fixed-t amplitude analysis (FT AA) and the single-energy partial-wave analysis (SE PWA). The two analyses are coupled in such a way that the results from FT AA are used as a constraint in SE PWA and vice versa in an iterative procedure. It cannot be proven, but it is extensively tested in πN elastic, fixed-t constrained SE PWA [15], and since then recommended for other processes.

Step 1: Constrained FT AA is performed by minimizing the form

$$X^2 = \chi^2_{\text{FTdata}} + \chi^2_{\text{cons}} + \Phi_{\text{conv}}, \tag{47}$$

where χ^2_{cons} is a constraining term given by

$$\chi^2_{\text{cons}} = q_{\text{cons}} \sum_{k=1}^{4} \sum_{i=1}^{N^E} \left[\frac{\text{Re } H_k(E_i, t)^{\text{fit}} - \text{Re } H_k(E_i, t)^{\text{cons}}}{\varepsilon_{k,i}^{\text{Re}}} \right]^2$$

$$+ q_{\text{cons}} \sum_{k=1}^{4} \sum_{i=1}^{N^E} \left[\frac{\text{Im } H_k(E_i, t)^{\text{fit}} - \text{Im } H_k(E_i, t)^{\text{cons}}}{\varepsilon_{k,i}^{\text{Im}}} \right]^2. \tag{48}$$

H_k^{cons} are helicity amplitudes from SE PWA of the previous iteration. In a first iteration, H_k^{cons} are calculated from the initial PWA solution (MAID). H_k^{fit} are values of helicity amplitudes H_k calculated from coefficients in Pietarinen's expansions, which are parameters of the fit. N_E is the number of energies for a given value of t, and q_{cons} is an adjustable weight factor. $\varepsilon_{k,i}^{\text{Re}}$ and $\varepsilon_{k,i}^{\text{Im}}$ are errors of real and imaginary parts of the corresponding helicity amplitudes. In our analysis, we take $\varepsilon_{k,i}^{\text{Re}} = \varepsilon_{k,i}^{\text{Im}} = 1$.

Step 2: Constrained SE PWA is performed by minimizing the form

$$X^2 = \chi^2_{\text{SEdata}} + \chi^2_{\text{FT}} + \Phi_{\text{trunc}}, \tag{49}$$

where χ^2_{FT} is a constraining term given by

$$\chi^2_{\text{FT}} = q_{\text{cons}} \sum_{k=1}^{4} \sum_{i=1}^{N^C} \left[\frac{\text{Re } H_k(E, \theta_i)^{\text{fit}} - \text{Re } H_k(E, \theta_i)^{\text{FT}}}{\varepsilon_{k,i}^{\text{Re}}} \right]^2$$

$$+ q_{\text{cons}} \sum_{k=1}^{4} \sum_{i=1}^{N^C} \left[\frac{\text{Im } H_k(E, \theta_i)^{\text{fit}} - \text{Im } H_k(E, \theta_i)^{\text{FT}}}{\varepsilon_{k,i}^{\text{Im}}} \right]^2. \tag{50}$$
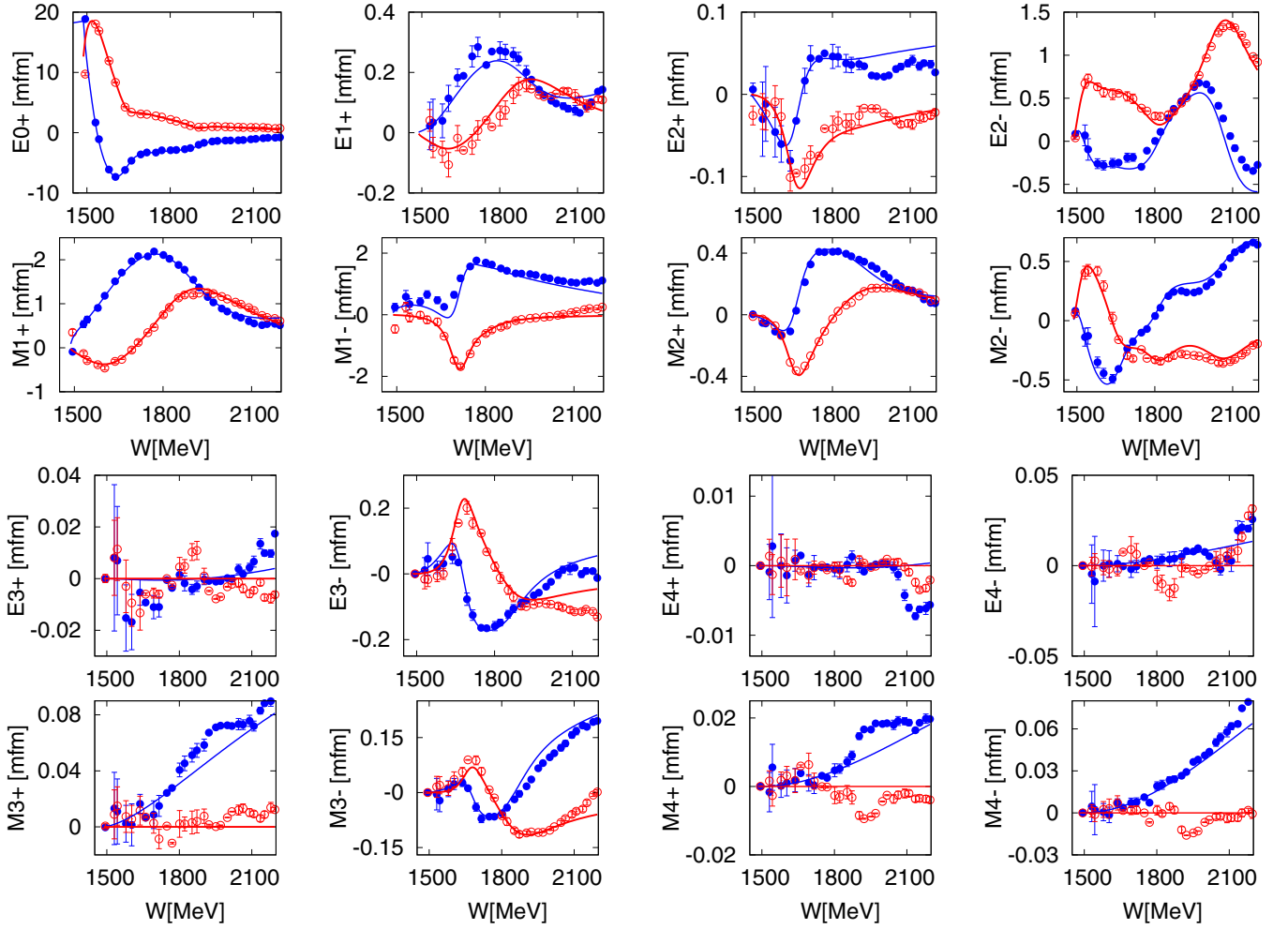
FIG. 13. Real (blue) and imaginary (red) parts of electric and magnetic multipoles up to $L = 4$ after the final iteration. The points are the result of the analytically constrained single-energy fit to the pseudodata and are compared to the multipoles of the underlying EtaMAID-2015 model, solution I, shown as solid lines.

H_k^{FT} are helicity amplitudes from FT AA of the previous iteration. H_k^{fit} are values of helicity amplitudes H_k calculated from multipoles of the SE PWA, which are parameters of the fit. N_C is the number of angles θ_i, corresponding to the t_i values from FT AA.

Step 3: Use resulting multipoles obtained in step 2, and calculate helicity amplitudes which serve as a constraint in step 1.

In summarizing our iterative procedure, we perform two different (initially independent) data analyses: first a FT AA,

where the energy values E are continous and t_i and θ_i values are discrete, and second a SE PWA, where the energy values E_i are discrete and θ and t values are continuous. Both are coupled via constraints, χ_{FT}^2 in SE PWA, Eq. (49), and χ_{cons}^2 in FT AA, Eq. (47). Both constraints are constructed in such a way that no further interpolation of the solutions are needed. For SE PWA constraint is calculated from coefficients in Pietarinen's expansion at discrete energies E_i, and for FT AA constraint is calculated from multipoles for discrete t_i values.

This procedure is illustrated in Fig. 4.

TABLE I. Experimental data from A2@MAMI and GRAAL used in our PWA.

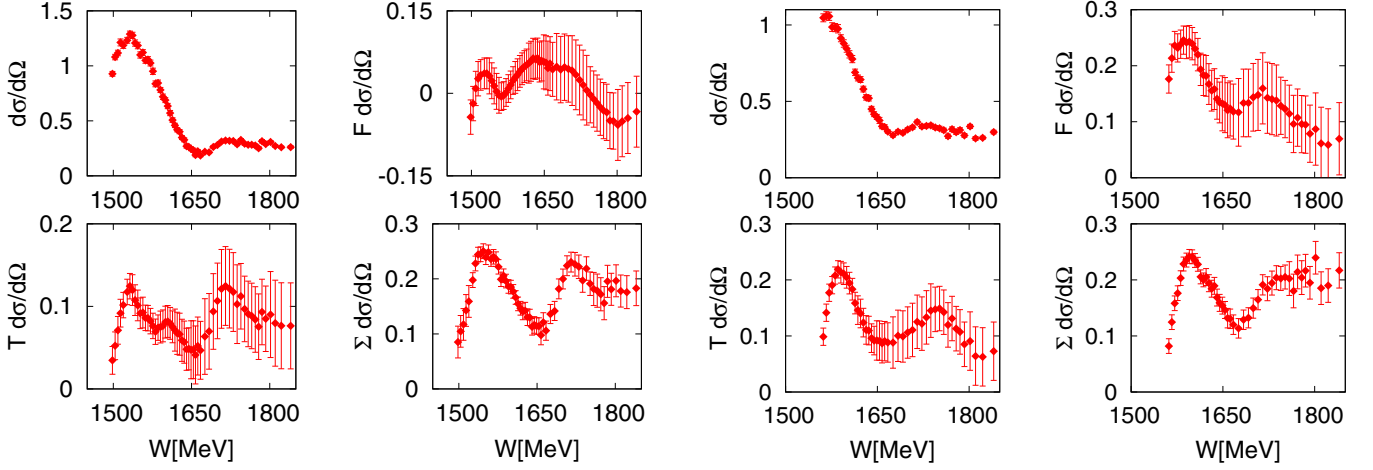| Obs	N	E_{lab} [MeV]	N_E	θ_{cm} [^{0}]	N_θ	Reference
σ_0	2400	710–1395	120	18–162	20	A2@MAMI(2010,2017) [16,17]
Σ	150	724–1472	15	40–160	10	GRAAL(2007) [19]
T	144	725–1350	12	24–156	12	A2@MAMI(2014) [18]
F	144	725–1350	12	24–156	12	A2@MAMI(2014) [18]

FIG. 14. Example of our interpolated fixed-*t* database for $t = -0.2\,\mathrm{GeV}^2$ and $t = -0.5\,\mathrm{GeV}^2$. The threshold values of the physical region are $W_{\mathrm{thr}} = 1486$ MeV for $t = -0.2\,\mathrm{GeV}^2$ and $W_{\mathrm{thr}} = 1554$ MeV for $t = -0.5\,\mathrm{GeV}^2$.

IV. STUDIES WITH PSEUDODATA

In this section, we study the potential impact of our method by analyzing pseudodata, which were generated numerically from multipoles of a recent EtaMAID model. Here we know exactly the input amplitudes and can compare them directly to the results obtained from fits of different sets of observables. We follow the following strategy:

(1) As a first step, we demonstrate that a fully unconstrained SE fit of even a complete set of observables does not give a unique solution. At each energy, we obtain a band of equivalent solutions, depending on the choice of the initial parameter values.

(2) We then perform a fit with fixed-*t* constraints according to the procedure described in Sec. III using the same complete set of observables from pseudodata as in the first step.

(3) Finally, we reduce the number of observables to four and use the same set which is available from real measurements at MAMI and GRAAL.

A. Input from pseudodata

We have generated all 16 observables from multipoles predicted by the EtaMAID-2015 model [32] (solution I). We randomize the unpolarized cross section by a normal distribution with a standard deviation of 0.1%. For the polarization observables, we first randomize the polarized cross sections again by a normal distribution with a standard deviation of 0.1% and calculate the observables as the difference between two polarization directions. The asymmetries are then obtained by division and error propagation. By this procedure, the unpolarized cross section obtains the highest precision, whereas polarization asymmetries obtain larger errors, especially when the asymmetries are small. This reflects better the situation of real experiments. However, here we still investigate the more or less ideal case with a precision which will not be
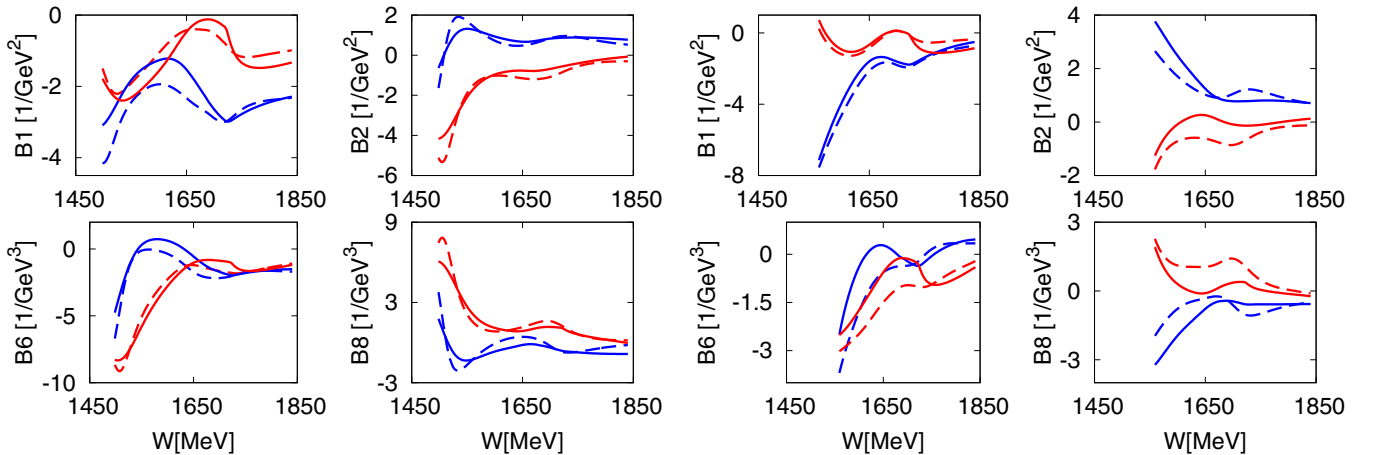

FIG. 15. Invariant amplitudes $B_1, B_2, B_6,$ and B_8 as functions of the total c.m. energy W at $t = -0.2\,\mathrm{GeV}^2$ (left) and $-0.5\,\mathrm{GeV}^2$ (right). The blue and red curves show real and imaginary parts of the amplitudes of solutions II (dashed) and III (solid) respectively.

FIG. 16. Helicity amplitudes H_1, H_2, H_3, and H_4 as functions of the total c.m. energy W at $t = -0.2 \text{ GeV}^2$ (left) and $t = -0.5 \text{ GeV}^2$ (right). The blue and red curves show real and imaginary parts of the amplitudes of solutions II (dashed) and III (solid) respectively.
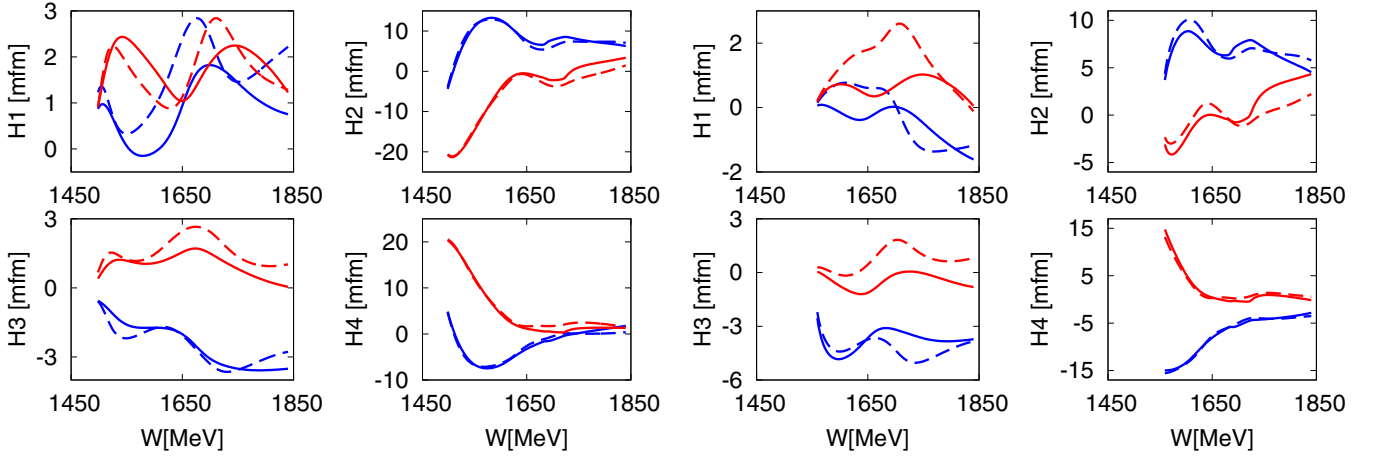
reached in real measurements of spin observables. We start our analysis using a complete set of observables which has to include double polarization observables with beam, target, and recoil polarization [5,43]. We have chosen the following set: $\{\sigma_0, \check{\Sigma}, \check{T}, \check{P}, \check{F}, \check{G}, \check{C}_{x'}, \check{O}_{x'}\}$.

For our procedure, we need the data at two different kinematic grids: energy and t $\{W_i, t_j\}$ for the fixed-t amplitude analysis, and energy and polar angle $\{W_i, \theta_k\}$ for the single-energy multipole fit. Our pseudodata sets were generated at 140 energies, each at 50 t values and 18 angles. Examples of these observables at two different energies can be found in Fig. 7.

B. Unconstrained fit with pseudodata

As first step, we have performed a fully unconstrained single-energy multipole fit, truncated to $L_{\max} = 5$, using the complete set of observables from pseudodata defined in Sec. IV A. We start the minimization procedure at initial values which were randomly distributed by 50% around the

true solution. In order to fix the overall energy-dependent phase, we fixed the phase of the E_{0+} multipole to the phase of the EtaMAID model, leaving 39 real parameters from 20 complex multipoles. The results of one of these fits are shown in Fig. 5. Even in this ideal case, a fully unconstrained fit does not result uniquely in the correct multipoles. At each energy, we find a band of equivalent solutions (similar χ^2) depending on the particular values chosen for the starting parameters of the fit. As the fits at each energy are independent from each other, the energy dependence of these solutions is discontinuous. For any other choice of initial parameter values, we obtain another, completely different, but still discrete set of multipoles. This observation can be explained in the following way. It can be shown, that in case of truncated data with highest angular momentum being $L_{\max}$ and very high precision, a SE PWA (TPWA) truncated to the same $L_{\max}$ gives a unique and continuous solution. If the data are not truncated and higher partial waves do contribute, a unique solution is not obtained, even using a complete set of infinitely precise data. A unique solution can, however, be restored if the higher partial waves,
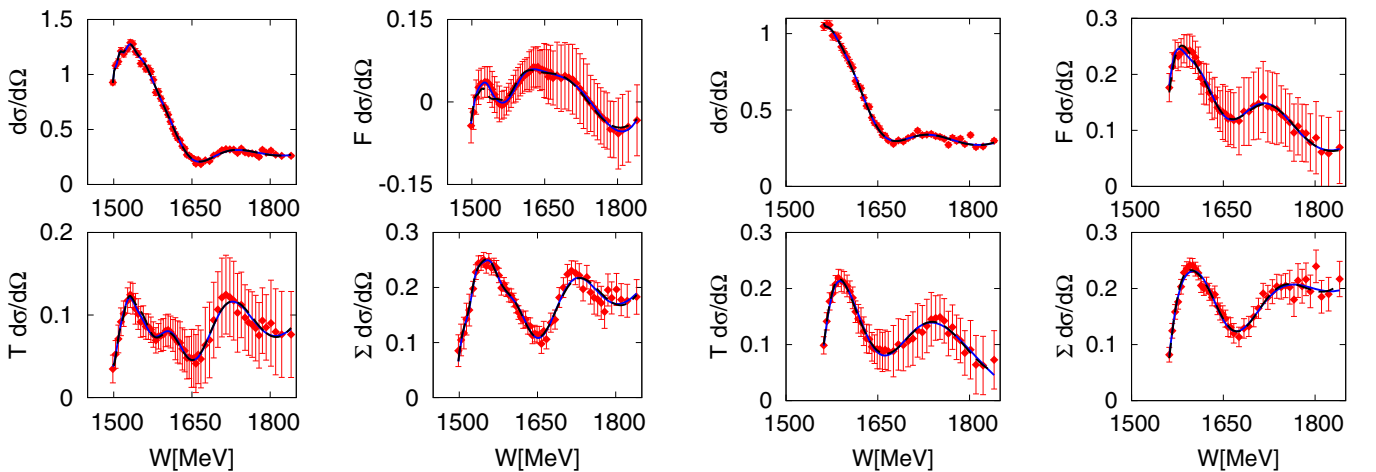

FIG. 17. Pietarinen fit of the interpolated data at $t = -0.2 \text{ GeV}^2$ and $t = -0.5 \text{ GeV}^2$. The dashed (black) and solid (blue) curves are the results starting with solutions II and III, respectively, and are on top of each other.
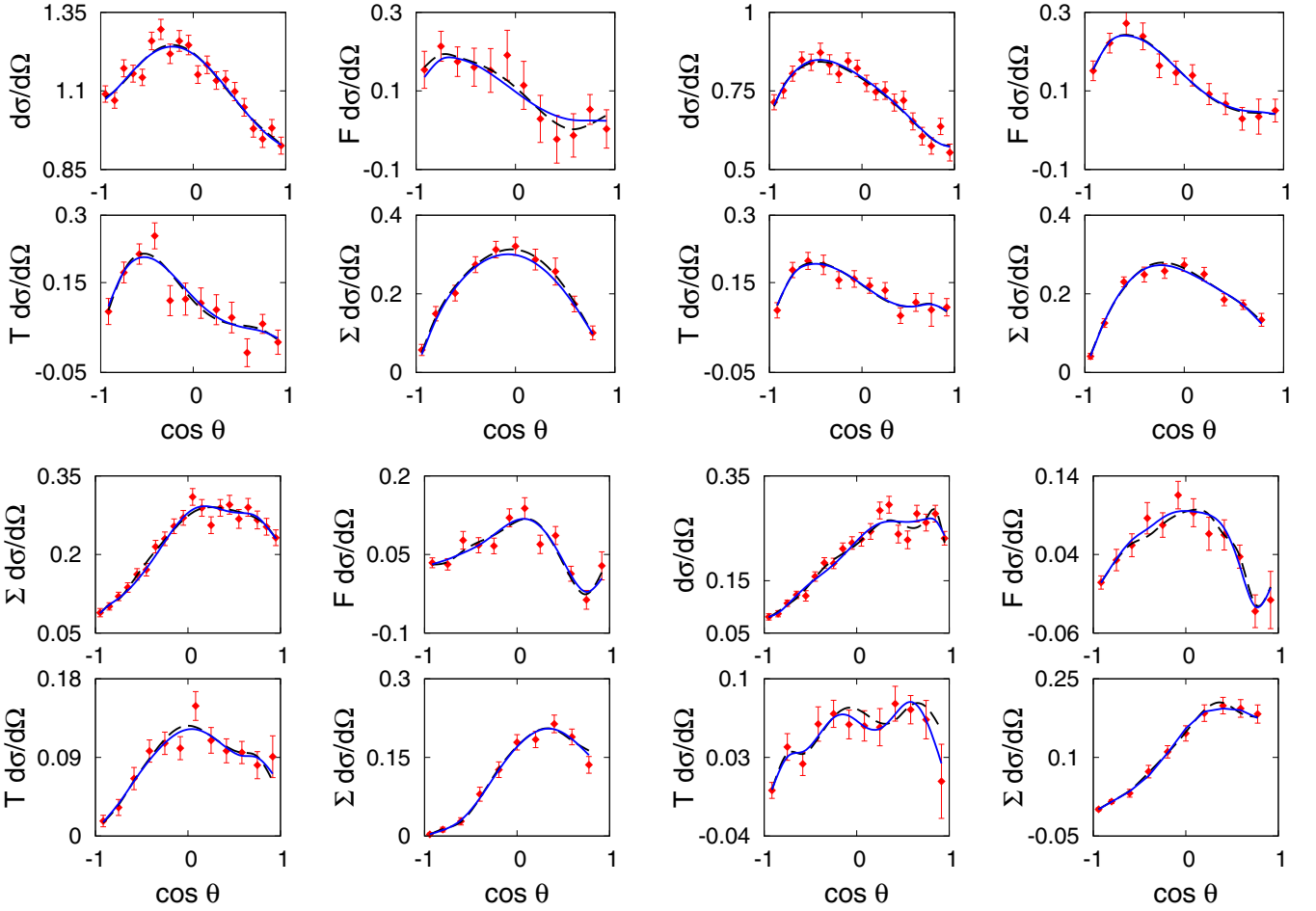
FIG. 18. Single-energy fit to the experimental data at $E = 818$ MeV ($W = 1554$ MeV) (top left) and $E = 898$ MeV ($W = 1602$ MeV) (top right) and at $E = 1191$ MeV ($W = 1765$ MeV) (bottom left) and $E = 1335$ MeV ($W = 1840$ MeV) (bottom right), using the analytical constraint of solutions II and III, drawn as dashed and solid lines, respectively.

$L > L_{\max}$, are known, e.g., from background terms. In practice, this ideal situation is approximately fulfilled only for charged pion photoproduction, where a sizable contribution of the background arises from the well-known pion pole contribution which can be calculated in a model-independent way. For other reactions like kaon or η photoproduction, the couplings of the Born terms are fairly unknown and also the t-channel contributions from vector mesons are important and model dependent.

Therefore, in η photoproduction, higher partial waves from background cannot be used as model-independent input in SE fits. However, a model-independent relation between SE fits at different energies can be provided by fixed-t analyticity.

C. Pseudodata analysis with fixed-t analyticity constraints

In the following, we describe the iterative procedure of successive amplitude analyses at fixed-t and multipole fits at fixed energy introduced in Sec. III.

Step 1: Fixed-t amplitude analysis. The complete set of eight observables $\sigma_0, \check{\Sigma}, \check{T}, \check{P}, \check{F}, \check{G}, \check{C}_{x'}, \check{O}_{x'}$ at 50 fixed-t values in the range of $-1.0 \, \text{GeV}^2 \leqslant t \leqslant -0.1 \, \text{GeV}^2$ were fitted. The

minimization is performed in terms of Pietarinen expansions according to Eq. (47). We start in minimization procedure at initial values which were randomly distributed by 50% around the true solution. Examples of these fits at $t = -0.2 \, \text{GeV}^2$ and $t = -0.5 \, \text{GeV}^2$ are shown in Fig. 6. With a typical number of $N \approx 20$ coefficients for each Pietarinen, a very precise description of all observables can be achieved. As a consequence, also all four underlying complex amplitudes, CGLN, and helicity amplitudes are perfectly reproduced up to an overall energy- and angle-dependent phase. Furthermore, it is important to note that in this case all possible 16 observables are described, including those which were not fitted. The helicity amplitudes obtained in this fit are now used as constraint in a SE PWA.

Step 2: A SE PWA fit is performed using constraints from step 1. The conditions for the single-energy partial-wave analysis are identical to those used in the unconstrained analysis; however, we did not fix the E_{0+} phase. We fit up to $L_{\max} = 5$ which corresponds to 20 complex multipoles or 40 real parameters. All multipoles for $L > 5$ are set to zero. The starting values of the fit parameters are again randomly chosen in a 50% range around the true solution.
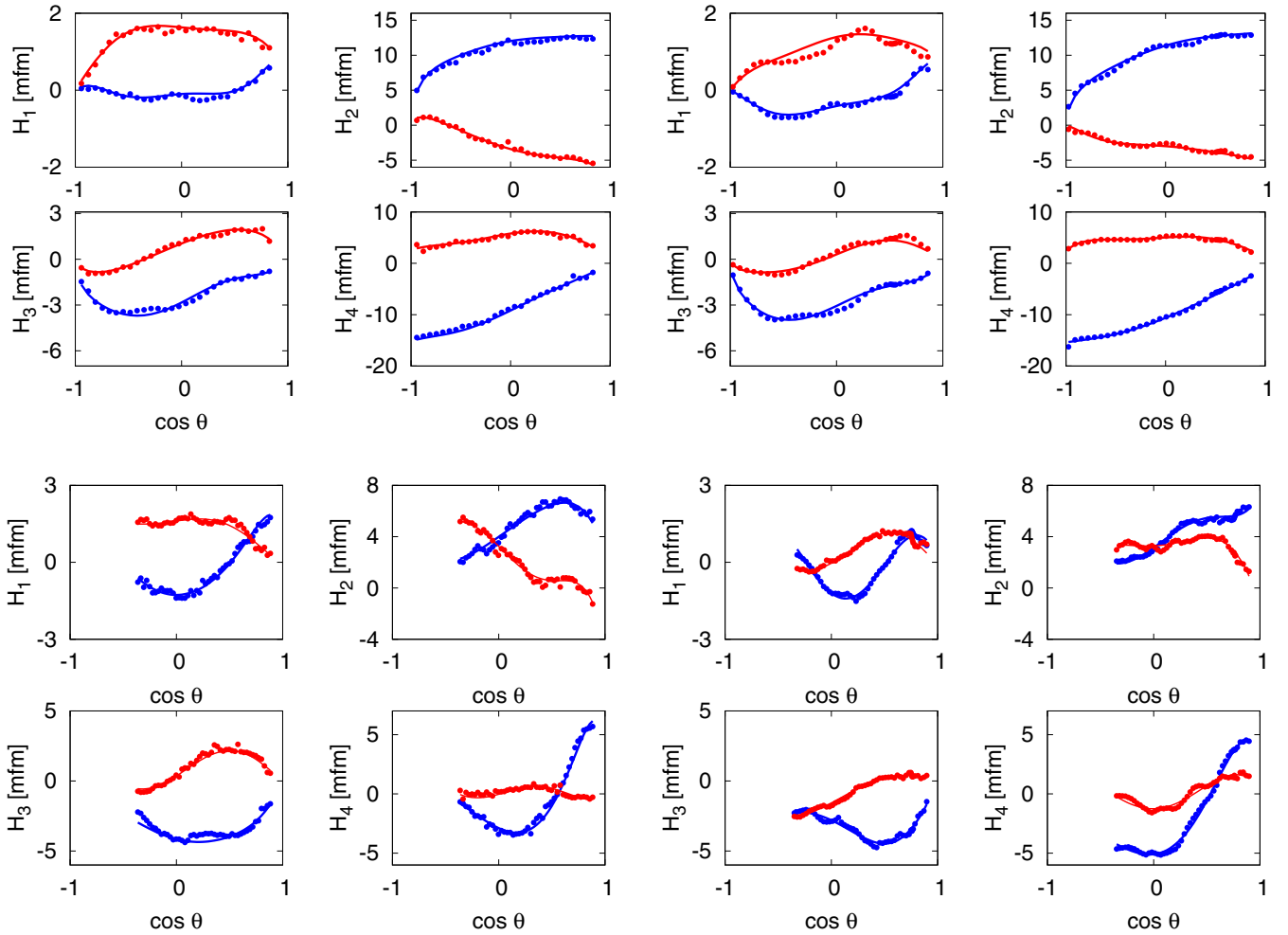
FIG. 19. Helicity amplitudes obtained by FT AA (in first iteration) using solutions II (left) and III (right) as constraints at fixed energies $W = 1602$ MeV (top) and $W = 1840$ MeV (bottom). The blue and red points show the result of the fixed-t analysis and are independent from point to point. The blue and red solid lines are obtained from the single-energy partial wave analysis and are continuous over the angular range. At the higher energy, the kinematical range is restricted due to the restrictions in the t value, $-1.0 \leqslant t \leqslant 0$.

The fits of the complete set of observables from pseudodata at $E = 800$ MeV ($W = 1543$ MeV) and $E = 1200$ MeV ($W = 1770$ MeV) are shown in Fig. 7. Again, as in step 1, all observables are perfectly described. As a consequence, again all four underlying complex amplitudes, CGLN, and helicity amplitudes are perfectly reproduced up to an overall energy- and angle-dependent phase. However, this phase has now changed compared to the solution from step 1.

Step 3: Further iterations and final solution. After only two iterative steps, no further change in the helicity amplitudes is observed. We conclude that the final solution is obtained. In Fig. 8, the helicity amplitudes $H_k(W, \cos\theta)$ of the final solution at $W = 1543$ MeV and $W = 1660$ MeV are compared to corresponding helicity amplitudes from previous FT amplitude analysis. All helicity amplitudes of the generating model are restored. The multipoles obtained in this fixed-t constrained SE PWA are compared to the input multipoles of the EtaMAID model in Fig. 9. Indeed, a unique solution was

obtained, which is in perfect agreement with the underlying model.

D. Pseudodata analysis with four observables and fixed-t analyticity constraints

As a final test with pseudodata, we reduce the number of observables to four. We repeat the iterative fitting procedure now using only pseudodata for $\sigma_0, \check{\Sigma}, \check{T}, \check{F}$, i.e., the same observables which have been measured experimentally. This set does not correspond to a complete experiment and, furthermore, it does not fulfill the completeness requirements of a TPWA as was found in Ref. [5]. Therefore, we cannot expect a unique solution.

Step 1: Fixed-t amplitude analysis. In the first step, again all four observables can be well described in the fixed-t amplitude analysis. Examples of fits at $t = -0.2$ GeV^2 and $t = -0.5$ GeV^2 are shown in Fig. 10.
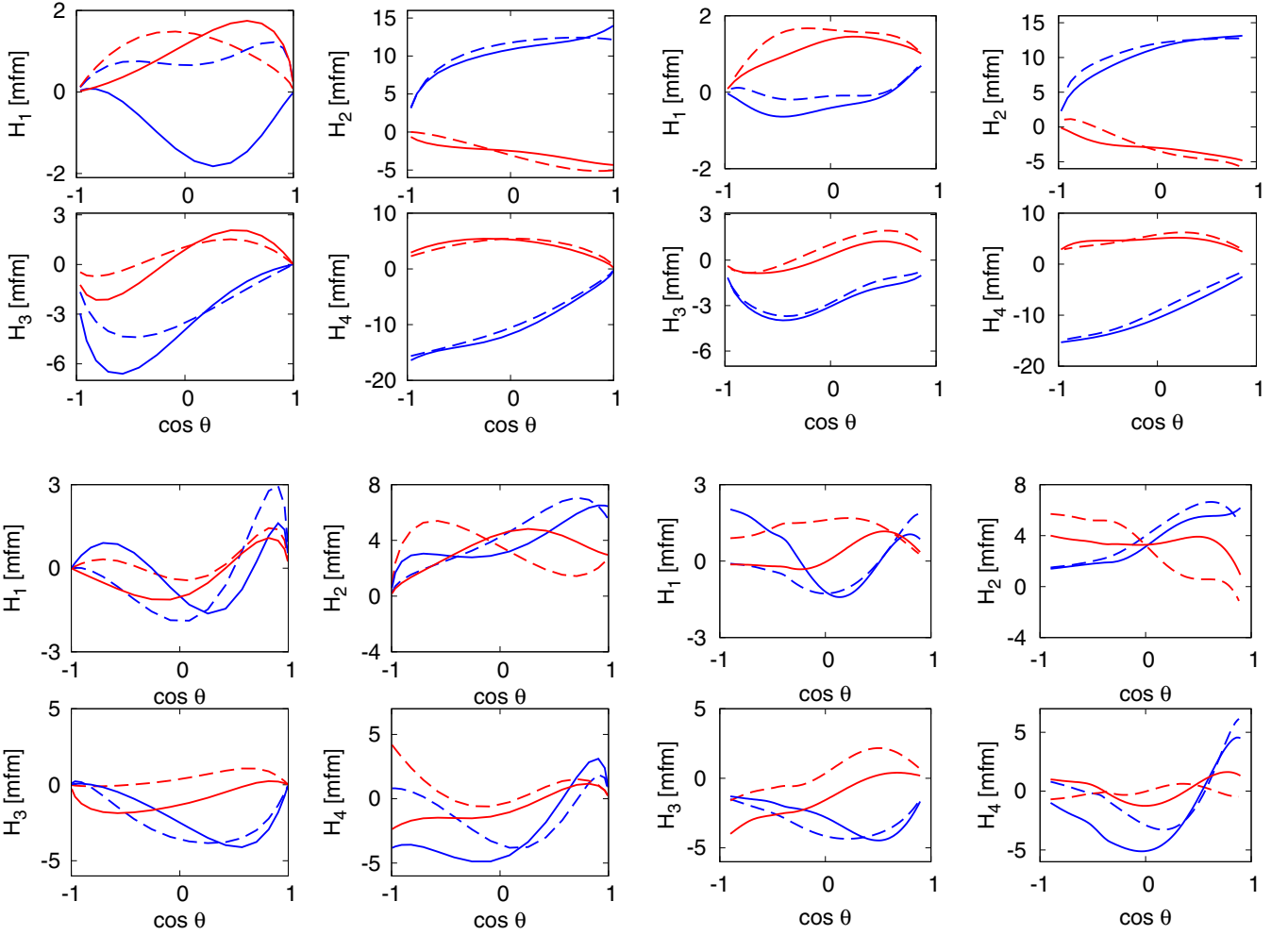
FIG. 20. Evolution of the helicity amplitudes at fixed energies $W = 1602$ MeV (top) and $W = 1840$ MeV (bottom) from the initial (left panel) to the final step (right panel) after three iterations using solutions II (dashed) and III (solid) as a constraint. The real parts of the amplitudes are shown in blue and the imaginary parts in red.

However, as the set of four observables does not form a complete experiment, we can now not expect that all other observables are described as well. Therefore, the helicity amplitudes, which are used as constraint in the following step, are not unique in the overall phase as was the case in the previous study with eight observables.

Step 2: A constrained SE fit using constraints of step 1. In single-energy partial-wave analysis, we again fitted 40 real parameters up to $L_{\max} = 5$. The results at $E = 1200$ MeV ($W = 1770$ MeV) and $E = 1460$ MeV ($W = 1900$ MeV) are shown in Fig. 11.

Again, the fitted observables, $\sigma_0, \check{\Sigma}, \check{T}, \check{F}$, are perfectly described. However, we cannot expect that also the remaining 12 observables, which were not fitted, are described. Figure 12 shows this comparison of these remaining 12 observables to the fit result. While at lower energies the prediction calculated from the fitted multipoles are quite good, at higher energies clear discrepancies are observed. The multipoles, obtained in the final iteration, are compared to the underlying model in Fig. 13. In contrast to fully unconstrained fits, we do find a solution, which is smooth in energy. However, in some

regions, the multipoles differ from the "true" values of the input model.

At lower energies, $W \leqslant 1800$ MeV, the SE PWA converges after the final iteration to the true solution, while at higher energies some multipoles deviate significantly. However, in principle these ambiguities can be resolved by adding further polarization observables as P or O_z (see Fig. 12).

V. RESULTS WITH EXPERIMENTAL DATA

In this section, we will apply our iterative procedure with fixed-t analyticity constraints to a partial-wave analysis of experimental data on η photoproduction. Unlike the very successful test with pseudodata, we have to consider some limitations by using real data. First of all, we do not have a complete data set with eight polarization observables available. This is, however, not stringently required. For a truncated partial-wave analysis, it was shown [5] that already a minimal set of four observables, e.g., $\{\sigma_0, \Sigma, F, H\}$ or $\{\sigma_0, T, P, F\}$, would be sufficient, providing that the observables are free of uncertainties. Even very small errors below 0.1% can lead
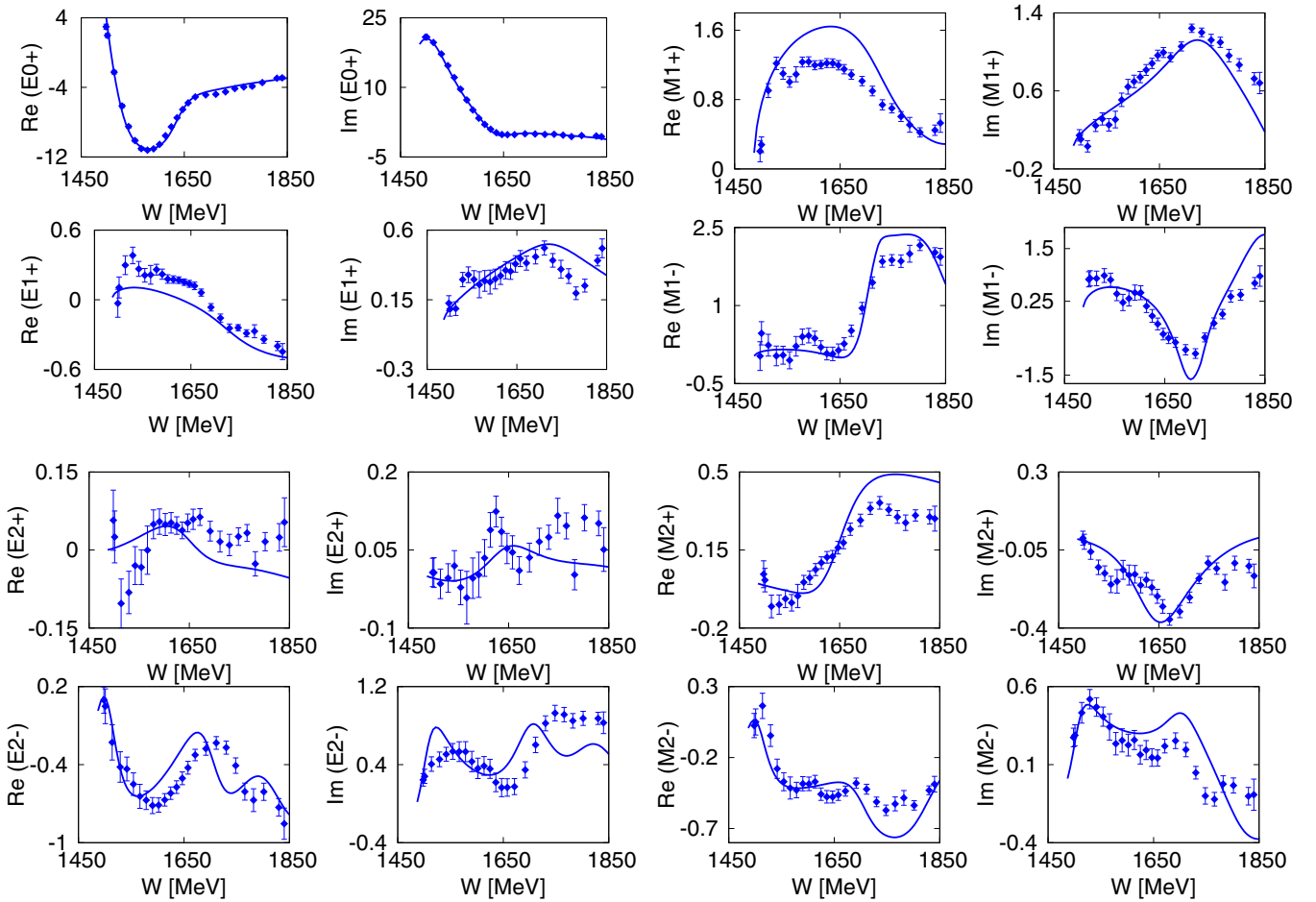
FIG. 21. Evolution of the S-, P-, and D-wave multipoles from the initial solutions II (full lines) to the final step (blue dots) after three iterations.

to multiple solutions. And this becomes more problematic when the truncation level increases, i.e., when L_{max} increases. In the ambiguity studies of Omelaenko [4,44], sets of five observables, as $\{\sigma_0, \Sigma, T, P, F\}$ were discussed, which, in numerical analysis, show up more robust than the minimal sets of four. Such sets will soon become available, when all data that are presently in progress are finally analyzed. Currently, we only have an incomplete data set $\{\sigma_0, \Sigma, T, F\}$ available, for which the limitations have already been discussed in the previous section by using pseudodata. A further limitation will always be the statistical and systematical uncertainties of real data, which will be much larger than in our pseudodata test. But with the expected database of all eight observables obtained with beam and target polarization, part of this deficiency can be compensated with more than four observables. The same is true for the limitation in kinematical coverage. The best coverage in energy and angles is obtained for unpolarized cross sections. But a very good coverage is also available for the polarization data that we will use, at least up to a total c.m. energy of $W = 1.85$ GeV.

A. η photoproduction database

In our partial-wave analysis with experimental data, we have used recent A2@MAMI data for unpolarized differential cross section σ_0, single target polarization asymmetry T, and double beam-target polarization with circular polarized photons F. In addition, we have used the GRAAL data for single-beam polarization Σ. For details, see Table I. There are additional data from CLAS [45,46] and from CBELSA [47], which we do not use in our analysis. At low energy, the cross-sectional data from MAMI have much better statistics, and the higher energies we did not analyze as our fixed-t method becomes more difficult at higher energies.

In our database, we have many more energy points for differential cross sections than for polarization observables (120 vs 15, 12, and 12). In order to avoid the differential cross-sectional dominance in our fitting procedure, we use the same kinematical points also for the polarization data. So, experimental values of double-polarization asymmetry F, target asymmetry T, and beam asymmetry Σ for given angles have to be interpolated at the energies where σ_0 are available. We have used a spline smoothing method [48], which was similarly applied in the Karlsruhe-Helsinki analysis KH80 [15]. Errors of interpolated data are taken to be equal to errors of nearest measured data points.

To impose fixed-t analyticity, we also have to create a database at fixed t using measured angular distributions at fixed s. A fixed-t data point requires a special combination
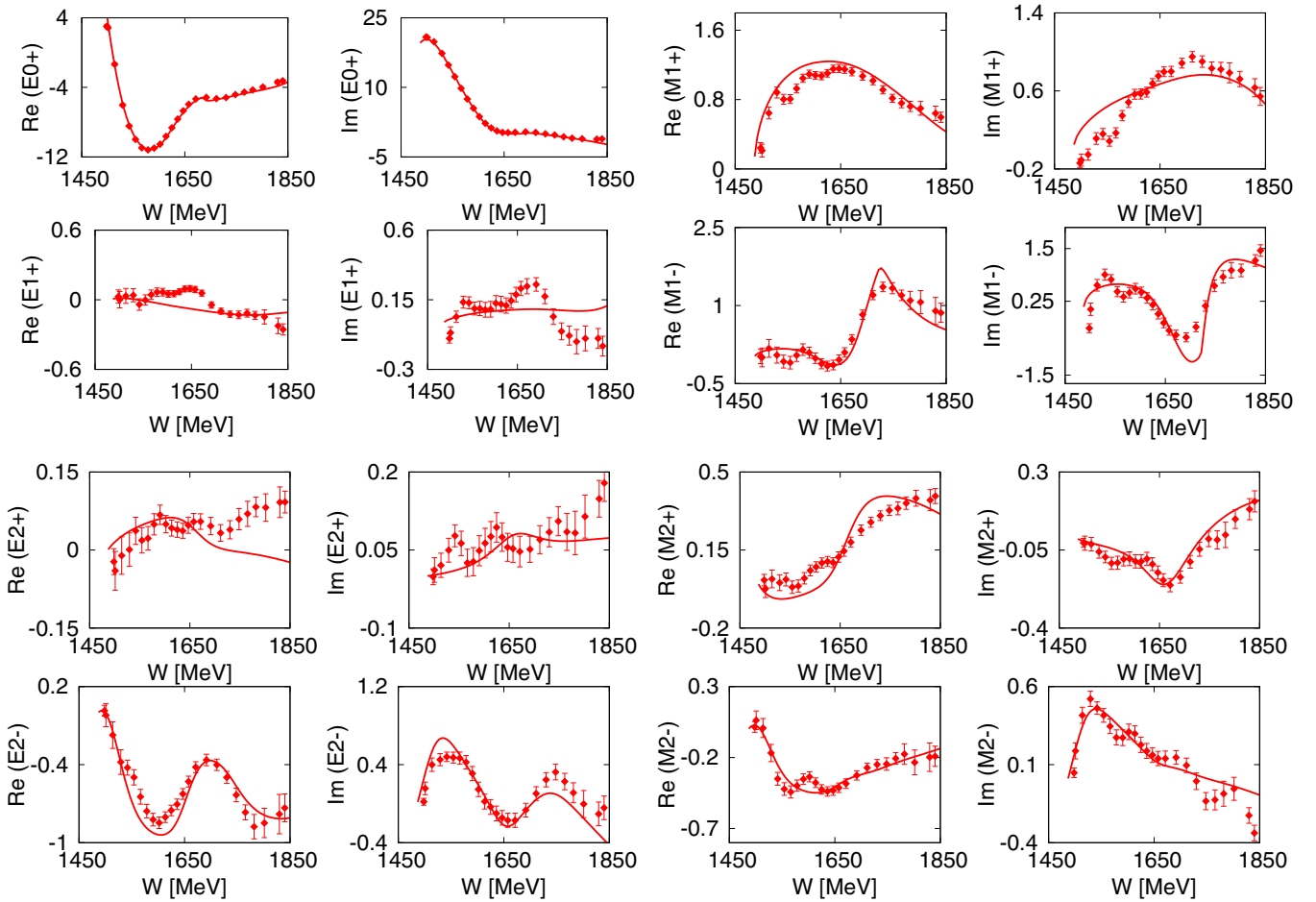
FIG. 22. Evolution of the S-, P-, and D-wave multipoles from the initial solutions III (full lines) to the final step (red dots) after three iterations.

of energy and angular points that in general cannot be found among directly measured data points. To obtain a data point in fixed t, we have to interpolate between nearby measured observable values and estimate the corresponding error. This is again done by the spline smoothing and interpolation method as described before.

Our fixed-t amplitude analysis is performed at t values in the range $-1.00\,\text{GeV}^2 < t < -0.1\,\text{GeV}^2$ with 20 equidistant t values. Examples of interpolated data at $t = -0.2\,\text{GeV}^2$ and $-0.5\,\text{GeV}^2$ are shown in Fig. 14. We note that the error bars for the polarization observables must be considered as error bands and the results of our minimization in the fixed-t analysis must not be taken as values of a χ^2 distribution.

In order to explore the model dependence of our solution, we start the analysis with two different MAID solutions, which we denote solution II (EtaMAID-2016 [33]) and solution III (EtaMAID-2017 [16]). To start an analysis, we randomize the starting values by 50% around the solutions II and III. In Fig. 15, we compare the invariant amplitudes from initial solutions II and III at $t = -0.2$ and $-0.5\,\text{GeV}^2$ and in Fig. 16 we compare the helicity amplitudes. The two EtaMAID solutions II and III are significantly different from each others. This can be seen, especially, where amplitudes become small. For the largest amplitudes, H_2 and H_4, where the S-wave

multipole dominates, in particular for low energies, the two models become much more similar.

These two starting solutions are expanded in Pietarinen series as described before and the Pietarinen coefficients $\{b_{ki}^{(1)}\}$, $\{b_{ki}^{(2)}\}$ are fitted to the fixed-t data. The results of the fits are shown in Fig. 17. With both initial solutions II and III, the fits agree very well with the data and cannot be distinguished in the plots. Generally, we want to remember that in an amplitude representation of the observables a continuum ambiguity exists. Therefore, even identical fits can still have very different underlying amplitudes. However, due to the Pietarinen representation of both amplitudes, fixed-t analyticity is obeyed by both solutions. The latter one is not generally true for any phase rotated set of amplitudes.

Figure 17 is the first step of the iterative minimization scheme outlined in Fig. 4. The solutions of the invariant amplitudes allow us to evaluate the helicity amplitudes at each energy, which is needed for the next step to perform the SE PWA in first iteration. This is shown in Fig. 18 at four different energies in the range of $W = 1554$–1840 MeV. The fit parameters in this minimization step are the complex electric and magnetic multipoles up to $L_{\max} = 5$.

With this first iteration, we can now compare helicity amplitudes from the FT AA analysis with those calculated with
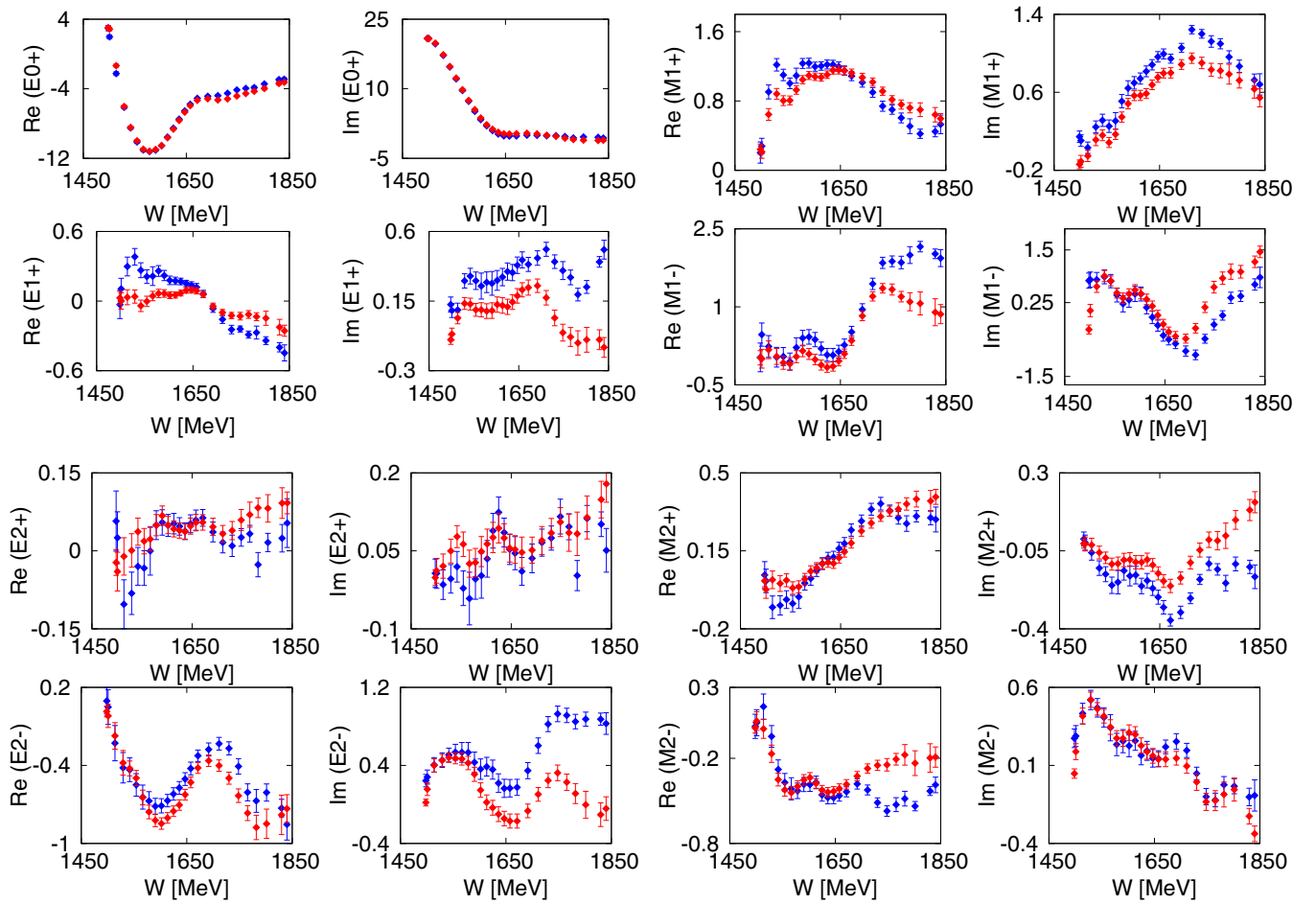
FIG. 23. Real and imaginary parts of the *S*-, *P*-, and *D*-wave multipoles obtained in the final step after three iterations using analytical constraints from helicity amplitudes obtained from initial solutions II (blue) and III (red).

the multipoles obtained in the SE PWA analysis. In Fig. 19, we make this comparison at $W = 1602$ MeV as a function of the scattering angle. The amplitudes obtained at fixed t values are principally discontinuous as the FT AA is independent at each different t value and therefore also at each different angle θ, while the multipole expansion of the helicity amplitudes are continuous functions of θ and shown as solid curves.

The iterative procedure outlined in Fig. 4 quickly converges after three iterations and the evolution of the helicity amplitudes obtained from the SE PWA is shown in Fig. 20. The amplitudes H_1 and H_3 show larger spreading between the two solutions and also a larger change during the iterative procedure compared to the amplitudes H_2 and H_4. The reason for this is that the changes of the four amplitudes are of the same size, but the magnitudes of H_2 and H_4 are much larger than for H_1 and H_3. Therefore, the effects are much more visible in H_1 and H_3. For these two amplitudes, it can also clearly be seen that the iterative procedure brings the two different initial solutions II and III much closer together after three iterations.

But also after the iterative procedure has converged, there remain residual differences between the final helicity amplitudes generated from solutions II and III. This results in different sets of partial waves (multipoles) when solutions II and III are used. In Figs. 21 and 22 these two sets of multipoles are

compared with the multipoles from their corresponding initial solutions. In both sets the dominant *S* wave almost does not change and agrees very well. For all other partial waves, an evolution from the initial to the final solution can be observed. In a few cases, especially from solution III, e.g., Re M_{1+}, and real and imaginary parts of E_{2-} and M_{2-} change only a little bit. A direct comparison of the two SE PWA is shown in Fig. 23. Again, almost no difference can be observed for the *S* wave and for most other partial waves the two solutions are consistent within their statistical uncertainties. However, for some partial waves considerable differences in certain kinematical regions show us clearly nonunique solutions, e.g., for Im E_{1+}, Im E_{2-}, and Re M_{2-}, just to mention the most obvious deviations.

There are different possible reasons for the nonunique partial-wave amplitudes shown in Fig. 23. First of all, our database is currently limited to only four observables, which gives a rather incomplete data set. This was already observed in our study with pseudodata and is demonstrated in Fig. 24, where we give predictions for nonfitted polarization observables of a complete set. Certainly in a complete experiment with a well-chosen set of eight observables we would have a guarantee that all possible observables would be well described, if a complete set is well fitted. If we now compare the predictions of nonfitted observables in the experimental
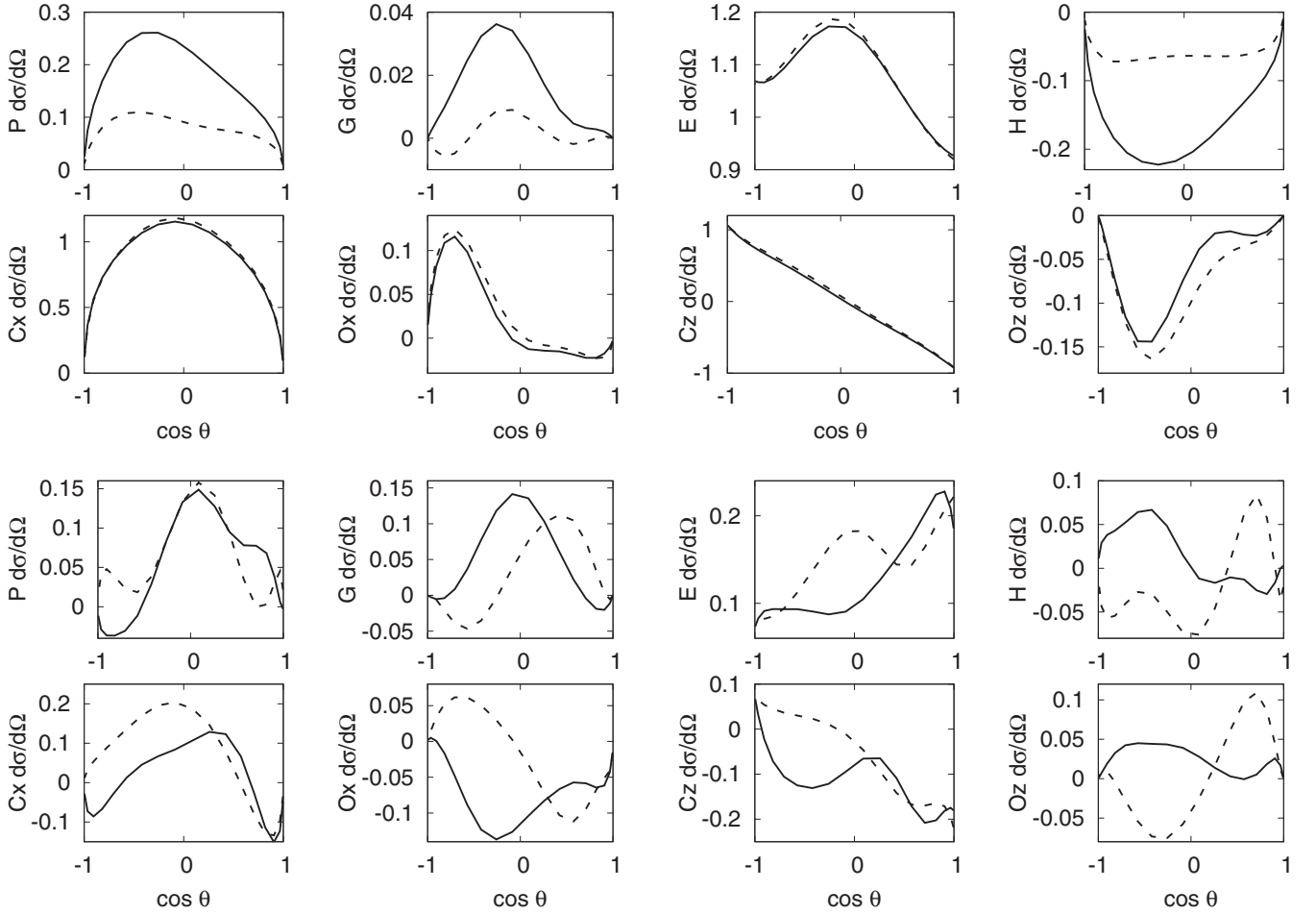
FIG. 24. Predictions from solutions II (dashed) and III (solid) for polarization observables that are not fitted $\{P, G, C_x, O_x\}$ (left) and $\{E, H, C_z, O_z\}$ (right) at two energies, $W = 1554$ MeV (top) and $W = 1765$ MeV (bottom). Together with our current experimental database $\{\sigma_0, \Sigma, T, F\}$, each additional group of four observables would make a complete experiment.

data analysis (Fig. 24) with the predictions in the pseudo data analysis (Fig. 12), we find large discrepancies in the observables P, G, and H. This arises most likely from the much larger uncertainties in the experimental data and from also possible systematic errors. Presumably, an inclusion of data from just one of them would again lead to a very good description of all observables with a data set of less than right observables and without any recoil polarization.

VI. SUMMARY AND CONCLUSIONS

Partial-wave series of meson photoproduction in the resonance region away from threshold converge rather slowly. Low partial waves, $L \lesssim 4$ are usually dominated by baryon resonance excitations, while higher partial waves obtain still significant contributions by Born terms and t-channel vector meson exchanges. Therefore, an unconstrained truncated partial-wave analysis with variation of all partial waves up to a maximal angular momentum L_{max} will not converge to unique solutions. With $L_{max} = 5$ a consistent database can well be fitted, but an increase by one more angular momentum can produce strong changes in lower partial waves. Further increase of partial waves will certainly lead to even better description of

the data, but it finally leads to the continuum ambiguity, where only the four underlying amplitudes are determined, but the partial waves become nonunique. Any phase transformation with energy- and angle-dependent phases will lead to a new (infinite) series of partial waves, where all of such sets can describe the database equally well.

Therefore, any PWA must be constrained. The most often used constraint is taken from a model that is fitted to the data in an energy-dependent way. Such a model will serve both for initial solutions in the SE fits and for higher partial waves. Such approaches are certainly strongly model dependent.

In this work, we have applied analytical constraints from fixed-t dispersion relations in partial wave analysis of η photoproduction data from threshold $W_{\eta,thr} = 1487$ MeV up to $W = 1850$ MeV. Following the ideas in the Karlsruhe-Helsinki πN PWA, we have developed a new method for partial-wave analysis of meson photoproduction data. In an iterative procedure, we perform fixed-t amplitude analyses using the Pietarinen expansion method and single-energy partial-wave analyses with a mutual support and constraint of each others, leading to a convergent partial-wave solution after about three iterations.

First, in an application with pseudodata, generated by the EtaMAID model, we have demonstrated that the method works

and converges to the underlying partial waves of the model, at least in the ideal case of a complete set of eight observables. The analysis of an incomplete set of the four observables consisting of the differential cross section, the single-spin target asymmetry T, and the beam target double polarization asymmetry F, leads to ambiguities which can be resolved adding another one or two selected observables.

Second, we have analyzed recent experimental data, which are still limited to the incomplete set of four observables described above. We find solutions for multipoles up to $L = 5$ which are continuous in energy. However, remaining ambiguities are found in particular at higher energies. New data from ELSA, JLab, and MAMI expected in the near future will help to resolve these ambiguities.

APPENDIX A: EXPANSION OF INVARIANT AMPLITUDES IN TERMS OF CGLN AMPLITUDES

The covariant amplitude A_i can be expressed by the CGLN amplitudes F_i as follows [49,50]:

$$A_1 = \mathcal{N}\left\{\frac{W + m_N}{W - m_N}\, F_1 - (E_f + m_N)\frac{F_2}{q} + \frac{m_N(t - \mu^2)}{(W - m_N)^2}\frac{F_3}{q} + \frac{m_N(E_f + m_N)(t - \mu^2)}{W^2 - m_N^2}\frac{F_4}{q^2}\right\},$$

$$A_2 = \frac{\mathcal{N}}{W - m_N}\left\{\frac{F_3}{q} - (E_f + m_N)\frac{F_4}{q^2}\right\},$$

$$A_3 = \frac{\mathcal{N}}{W - m_N}\left\{F_1 + (E_f + m_N)\frac{F_2}{q} + \left[W + m_N + \frac{t - \mu^2}{2(W - m_N)}\right]\frac{F_3}{q}\right.$$
$$\left. + \left[W - m_N + \frac{t - \mu^2}{2(W + m_N)}\right](E_f + m_N)\frac{F_4}{q^2}\right\},$$

$$A_4 = \frac{\mathcal{N}}{W - m_N}\left\{F_1 + (E_f + m_N)\frac{F_2}{q} + \frac{t - \mu^2}{2(W - m_N)}\frac{F_3}{q} + \frac{t - \mu^2}{2(W + m_N)}(E_f + m_N)\frac{F_4}{q^2}\right\}, \tag{A1}$$

where $\mathcal{N} = 4\pi/\sqrt{(E_i + m_N)(E_f + m_N)}$.

APPENDIX B: EXPANSION OF CGLN AMPLITUDES IN TERMS OF INVARIANT AMPLITUDES

The CGLN amplitudes are obtained from the invariant amplitudes A_i by the following equations:

$$F_1 = \frac{W - m_N}{8\pi\, W}\sqrt{(E_i + m_N)(E_f + m_N)}\left[A_1 + (W - m_N)\,A_4 - \frac{2m_N\nu_B}{W - m_N}(A_3 - A_4)\right],$$

$$F_2 = \frac{W + m_N}{8\pi\, W}\, q\,\sqrt{\frac{E_i - m_N}{E_f + m_N}}\left[-A_1 + (W + m_N)\,A_4 - \frac{2m_N\nu_B}{W + m_N}(A_3 - A_4)\right],$$

$$F_3 = \frac{W + m_N}{8\pi\, W}\, q\,\sqrt{(E_i - m_N)(E_f + m_N)}\left[(W - m_N)\,A_2 + A_3 - A_4\right],$$

$$F_4 = \frac{W - m_N}{8\pi\, W}\, q^2\,\sqrt{\frac{E_i + m_N}{E_f + m_N}}\left[-(W + m_N)\,A_2 + A_3 - A_4\right], \tag{B1}$$

with $\nu_B = (t - \mu^2)/(4m_N)$.

APPENDIX C: OBSERVABLES EXPRESSED IN CGLN AMPLITUDES

Spin observables expressed in CGLN amplitudes

$$\sigma_0 = \text{Re}\,\{F_1^* F_1 + F_2^* F_2 + \sin^2\theta\,(F_3^* F_3/2 + F_4^* F_4/2 + F_2^* F_3 + F_1^* F_4 + \cos\theta\, F_3^* F_4) - 2\cos\theta\, F_1^* F_2\}\rho, \tag{C1}$$

$$\check{\Sigma} = -\sin^2\theta\,\text{Re}\,\{(F_3^* F_3 + F_4^* F_4)/2 + F_2^* F_3 + F_1^* F_4 + \cos\theta\, F_3^* F_4\}\rho, \tag{C2}$$

$$\check{T} = \sin\theta\,\text{Im}\,\{F_1^* F_3 - F_2^* F_4 + \cos\theta\,(F_1^* F_4 - F_2^* F_3) - \sin^2\theta\, F_3^* F_4\}\rho, \tag{C3}$$

$$\check{P} = -\sin\theta\,\text{Im}\,\{2F_1^* F_2 + F_1^* F_3 - F_2^* F_4 - \cos\theta\,(F_2^* F_3 - F_1^* F_4) - \sin^2\theta\, F_3^* F_4\}\rho, \tag{C4}$$

$$\check{E} = \text{Re}\,\{F_1^* F_1 + F_2^* F_2 - 2\cos\theta\, F_1^* F_2 + \sin^2\theta\,(F_2^* F_3 + F_1^* F_4)\}\rho, \tag{C5}$$

$$\check{F} = \sin\theta\,\text{Re}\,\{F_1^* F_3 - F_2^* F_4 - \cos\theta\,(F_2^* F_3 - F_1^* F_4)\}\rho, \tag{C6}$$

TABLE II. Spin observables expressed by helicity amplitudes in the notation of Barker [2] and Walker [51]. A phase space factor q/k has been omitted in all expressions. The differential cross section is given by σ_0 and the spin observables $\check{O}_i$ are obtained from the spin asymmetries A_i by $\check{O}_i = A_i \sigma_0$.

Observable	Helicity representation	Type
σ_0	$\frac{1}{2}(\lvert H_1\rvert^2 + \lvert H_2\rvert^2 + \lvert H_3\rvert^2 + \lvert H_4\rvert^2)$	
$\check{\Sigma}$	$\mathrm{Re}(H_1 H_4^* - H_2 H_3^*)$	$\mathcal{S}$
$\check{T}$	$\mathrm{Im}(H_1 H_2^* + H_3 H_4^*)$	(single spin)
$\check{P}$	$-\mathrm{Im}(H_1 H_3^* + H_2 H_4^*)$	
$\check{G}$	$-\mathrm{Im}(H_1 H_4^* + H_2 H_3^*)$	
$\check{H}$	$-\mathrm{Im}(H_1 H_3^* - H_2 H_4^*)$	$\mathcal{BT}$
$\check{E}$	$\frac{1}{2}(-\lvert H_1\rvert^2 + \lvert H_2\rvert^2 - \lvert H_3\rvert^2 + \lvert H_4\rvert^2)$	(beam–target)
$\check{F}$	$\mathrm{Re}(H_1 H_2^* + H_3 H_4^*)$	
$\check{O}_{x'}$	$-\mathrm{Im}(H_1 H_2^* - H_3 H_4^*)$	
$\check{O}_{z'}$	$\mathrm{Im}(H_1 H_4^* - H_2 H_3^*)$	$\mathcal{BR}$
$\check{C}_{x'}$	$-\mathrm{Re}(H_1 H_3^* + H_2 H_4^*)$	(beam-recoil)
$\check{C}_{z'}$	$\frac{1}{2}(-\lvert H_1\rvert^2 - \lvert H_2\rvert^2 + \lvert H_3\rvert^2 + \lvert H_4\rvert^2)$	
$\check{T}_{x'}$	$\mathrm{Re}(H_1 H_4^* + H_2 H_3^*)$	
$\check{T}_{z'}$	$\mathrm{Re}(H_1 H_2^* - H_3 H_4^*)$	$\mathcal{TR}$
$\check{L}_{x'}$	$-\mathrm{Re}(H_1 H_3^* - H_2 H_4^*)$	(target-recoil)
$\check{L}_{z'}$	$\frac{1}{2}(\lvert H_1\rvert^2 - \lvert H_2\rvert^2 - \lvert H_3\rvert^2 + \lvert H_4\rvert^2)$	

$$\check{G} = \sin^2\theta\,\mathrm{Im}\{F_2^* F_3 + F_1^* F_4\}\rho, \tag{C7}$$

$$\check{H} = \sin\theta\,\mathrm{Im}\{2F_1^* F_2 + F_1^* F_3 - F_2^* F_4 + \cos\theta\,(F_1^* F_4 - F_2^* F_3)\}\rho, \tag{C8}$$

$$\check{C}_{x'} = \sin\theta\,\mathrm{Re}\{F_1^* F_1 - F_2^* F_2 - F_2^* F_3 + F_1^* F_4 - \cos\theta\,(F_2^* F_4 - F_1^* F_3)\}\rho, \tag{C9}$$

$$\check{C}_{z'} = \mathrm{Re}\{2F_1^* F_2 - \cos\theta\,(F_1^* F_1 + F_2^* F_2) + \sin^2\theta\,(F_1^* F_3 + F_2^* F_4)\}\rho, \tag{C10}$$

$$\check{O}_{x'} = \sin\theta\,\mathrm{Im}\{F_2^* F_3 - F_1^* F_4 + \cos\theta\,(F_2^* F_4 - F_1^* F_3)\}\rho, \tag{C11}$$

$$\check{O}_{z'} = -\sin^2\theta\,\mathrm{Im}\{F_1^* F_3 + F_2^* F_4\}\rho, \tag{C12}$$

$$\check{L}_{x'} = -\sin\theta\,\mathrm{Re}\{F_1^* F_1 - F_2^* F_2 - F_2^* F_3 + F_1^* F_4 + \sin^2\theta\,(F_4^* F_4 - F_3^* F_3)/2 + \cos\theta\,(F_1^* F_3 - F_2^* F_4)\}\rho, \tag{C13}$$

$$\check{L}_{z'} = \mathrm{Re}\{2F_1^* F_2 - \cos\theta\,(F_1^* F_1 + F_2^* F_2) + \sin^2\theta\,(F_1^* F_3 + F_2^* F_4 + F_3^* F_4) + \cos\theta\sin^2\theta\,(F_3^* F_3 + F_4^* F_4)/2\}\rho, \tag{C14}$$

$$\check{T}_{x'} = -\sin^2\theta\,\mathrm{Re}\{F_1^* F_3 + F_2^* F_4 + F_3^* F_4 + \cos\theta\,(F_3^* F_3 + F_4^* F_4)/2\}\rho, \tag{C15}$$

$$\check{T}_{z'} = \sin\theta\,\mathrm{Re}\{F_1^* F_4 - F_2^* F_3 + \cos\theta\,(F_1^* F_3 - F_2^* F_4) + \sin^2\theta\,(F_4^* F_4 - F_3^* F_3)/2\}\rho, \tag{C16}$$

with $\check{\Sigma} = \Sigma\,\sigma_0$ etc. and $\rho = q/k$. $\tag{C17}$

APPENDIX D: POLARIZATION OBSERVABLES IN TERMS OF HELICITY AMPLITUDES

The 16 polarization observables of pseudoscalar photoproduction fall into four groups, single spin with unpolarized cross section included and beam-target, beam-recoil, and target-recoil observables. The simplest representation of these observables is given in terms of helicity amplitudes (see Table II).

[1] V. Crede and W. Roberts, Rept. Prog. Phys. **76**, 076301 (2013).

[2] I. S. Barker, A. Donnachie, and J. K. Storrow, Nucl. Phys. B **95**, 347 (1975).

[3] A. Svarc *et al.*, arXiv:1706.03211 [nucl-th].

[4] Y. Wunderlich, R. Beck, and L. Tiator, Phys. Rev. C **89**, 055203 (2014).

[5] R. L. Workman, L. Tiator, Y. Wunderlich, M. Döring, and H. Haberzettl, Phys. Rev. C **95**, 015206 (2017).

[6] L. Tiator, R. L. Workman, Y. Wunderlich, and H. Haberzettl, Phys. Rev. C **96**, 025210 (2017).

[7] J. E. Bowcock and H. Burkhardt, Rep. Prog. Phys. **38**, 1099 (1975).

[8] O. Hanstein, D. Drechsel, and L. Tiator, Nucl. Phys. A **632**, 561 (1998).

[9] R. Beck, H. P. Krahn, J. Ahrens, J. R. M. Annand, H. J. Arends, G. Audit, A. Braghieri, N. d'Hose, D. Drechsel, O. Hanstein *et al.*, Phys. Rev. C **61**, 035204 (2000).

[10] D. Hornidge *et al.* (A2 and CB-TAPS Collaborations), Phys. Rev. Lett. **111**, 062004 (2013).

[11] I. G. Aznauryan, Phys. Rev. C **68**, 065204 (2003).

[12] I. G. Aznauryan, Phys. Rev. C **67**, 015209 (2003).

[13] S. S. Kamalov, L. Tiator, D. Drechsel, R. A. Arndt, C. Bennhold, I. I. Strakovsky, and R. L. Workman, Phys. Rev. C **66**, 065206 (2002).

[14] A. M. Sandorfi, S. Hoblit, H. Kamano, and T.-S. H. Lee, J. Phys. G **38**, 053001 (2011).

[15] G. Höhler, in *Pion Nucleon Scattering*, Landolt-Börnstein Vol. I/9b2, edited by H. Schopper (Springer, Verlag, 1983).

[16] V. L. Kashevarov *et al.*, Phys. Rev. Lett. **118**, 212001 (2017).

[17] E. F. McNicoll *et al.* (Crystal Ball at MAMI Collaboration), Phys. Rev. C **82**, 035208 (2010); **84**, 029901(E) (2011).

[18] C. S. Akondi *et al.* (A2 Collaboration at MAMI), Phys. Rev. Lett. **113**, 102001 (2014).

[19] O. Bartalini *et al.* (GRAAL Collaboration), Eur. Phys. J. A **33**, 169 (2007).

[20] W.-T. Chiang, S. N. Yang, L. Tiator, and D. Drechsel, Nucl. Phys. A **700**, 429 (2002).

[21] W.-T. Chiang, S. N. Yang, L. Tiator, M. Vanderhaeghen, and D. Drechsel, Phys. Rev. C **68**, 045202 (2003).

[22] V. A. Tryasuchev, Eur. Phys. J. A **22**, 97 (2004).

[23] V. A. Tryasuchev, B. A. Alekseev, V. S. Yakovleva, and A. G. Kondratyeva, Russ. Phys. J. **59**, 359 (2016).

[24] M. W. Paris and R. L. Workman, Phys. Rev. C **82**, 035202 (2010).

[25] R. Beck, E. Klempt, V. A. Nikonov, A. V. Sarantsev, and U. Thoma, Eur. Phys. J. A **48**, 88 (2012).

[26] A. V. Anisovich, E. Klempt, B. Krusche, V. A. Nikonov, A. V. Sarantsev, U. Thoma, and D. Werthmüller, Eur. Phys. J. A **51**, 72 (2015).

[27] V. Shklyar, H. Lenske, and U. Mosel, Phys. Lett. B **650**, 172 (2007).

[28] D. Rönchen, M. Döring, H. Haberzettl, J. Haidenbauer, U.-G. Meißner, and K. Nakayama, Eur. Phys. J. A **51**, 70 (2015).

[29] A. Sibirtsev, J. Haidenbauer, S. Krewald, and U.-G. Meißner, Eur. Phys. J. A **46**, 359 (2010).

[30] V. L. Kashevarov, M. Ostrick, and L. Tiator, Phys. Rev. C **96**, 035207 (2017).

[31] J. Nys, V. Mathieu, C. Fernandez-Ramirez, A. N. Blin, A. Jackura, M. Mikhasenko, A. Pilloni, A. P. Szczepaniak, G. Fox, and J. Ryckebusch (JPAC Collaboration), Phys. Rev. D **95**, 034014 (2017).

[32] V. L. Kashevarov, L. Tiator, and M. Ostrick, Bled Workshops Phys. **16**, No. 1 (2015) 9.

[33] V. L. Kashevarov, L. Tiator, and M. Ostrick (for A2 Collaboration at MAMI), JPS Conf. Proc. **13**, 020029 (2017).

[34] G. F. Chew, M. L. Goldberger, F. E. Low, and Y. Nambu, Phys. Rev. **106**, 1337 (1957).

[35] J. D. Bjorken and S. D. Drell, *Relativistic Quantum Fields*, (McGraw-Hill, New York, 1965).

[36] G. F. Chew, M. L. Goldberger, F. E. Low, and Y. Nambu, Phys. Rev. **106**, 1345 (1957).

[37] E. Pietarinen, Nuovo Cimento Soc. Ital. Fis. A **12**, 522 (1972).

[38] E. Pietarinen, Nucl. Phys. B **107**, 21 (1976).

[39] G. Höhler *et al.*, *Handbook of Pion-Nucleon Scattering*, Physics Data 12-1 (Fachinformationszentrum, Karlsruhe, 1979).

[40] J. Hamilton and J. L. Petersen, *New Development in Dispersion Theory*, Vol. 1 (Nordita, Copenhagen, 1973).

[41] J. Landay, M. Döring, C. Fernandez-Ramirez, B. Hu, and R. Molina, Phys. Rev. C **95**, 015203 (2017).

[42] B. Pasquini, D. Drechsel, and L. Tiator, Eur. Phys. J. A **27**, 231 (2006).

[43] W. T. Chiang and F. Tabakin, Phys. Rev. C **55**, 2054 (1997).

[44] A. S. Omelaenko, Yad. Fiz. **34**, 730 (1981) [Sov. J. Nucl. Phys. **34**, 406 (1981)].

[45] M. Dugger *et al.* (CLAS Collaboration), Phys. Rev. Lett. **89**, 222002 (2002).

[46] M. Williams *et al.* (CLAS Collaboration), Phys. Rev. C **80**, 045213 (2009).

[47] V. Crede *et al.* (CBELSA/TAPS Collaboration), Phys. Rev. C **80**, 055202 (2009).

[48] C. de Boor, *A Practical Guide to Splines* (Springer-Verlag, Heidelberg, 2001).

[49] P. Dennery, Phys. Rev. **124**, 2000 (1961).

[50] F. A. Berends, A. Donnachie, and D. L. Weaver, Nucl. Phys. B **4**, 1 (1967).

[51] R. L. Walker, Phys. Rev. **182**, 1729 (1969).